UNIVERSITY OF CANTERBURY

Florbetaben Amyloid Imaging for cognitive impairment in Parkinson's disease

Author:
Guneet KAUR

Supervisor:
Dr. Tracy MELZER
Dr. Steven MARSH

A thesis submitted in fulfillment of the requirements
for the degree of Master of Science
in the

College of Science
Department of Physics and Astronomy

February 26, 2016

Abstract

Objective: To determine using amyloid Positron Emission Tomographic (PET) imaging, whether amyloid burden indicated by Florbetaben (FBB) radiotracer, could predict cognitive decline in the Parkinson's disease individuals with Mild cognitive impairment (PD-MCI).

Methods: In study, movement disorder society (MDS) criteria were used to classify 50 participant with PD-MCI. All subjects underwent clinical evaluation, Structural 3T Magnetic resonance imaging and FBB PET imaging, along with cognitive assessments. The PET images were assessed clinically and the Standard uptake value ratio (SUVRs) were obtained for Region of interest (ROI) analysis, linear regression and multivariate analysis to asses association with cognitive and clinical measure.

Results: At baseline, among the 50 scans, 22 $\%$ clinically FBB-positive. The Group-by-Cognition showed an association between amyloid deposition in regions: neocortical, frontal and temporal cortex, anterior and posterior cingulate, precuneus and putamen with the global cognitive Z score, MoCa and Parkinson's disease dementia "risk" score (PDDRS). We also the pattern of amyloid accumulation in PD-MCI using multivariate analysis (principal Component analysis). We showed an association between our principal components with the clinical classification of positivity and the neuropsychological score. PCs showed worsening of cognitive impairment in the clinically FBB positive group. In the context of FBB negative group there was no association with the cognitive decline.

Conclusions: FBB-PET imaging allows $in\ vivo$ visualization of amyloid deposition in PD-MCI. At baseline measurements, our study show that amyloid accumulation could potential contribute to cognitive deterioration in PD-MCI.

Acknowledgements

Firstly, I would like to express my sincere gratitude to Dr.Tracy R Melzer for the continuous support and guidance through out the course of my project and thesis, for his patience, motivation and immense knowledge. His guidance helped me through out the course of my project and writing of this thesis.

I would also like to thank Dr. Steven Marsh, for his insightful comments, encouragement and support throughout the course of my masters degree.

My sincere thanks goes to Dr.Ross J Keenan for providing me with the clinical Amyloid diagnosis report for all fifty participant in short period of time.

I would also like to thank the Southern cross radiology team for working on providing us with PET Scans weekly. In particular, I would like to thank Clare Steven, for guiding me through image reconstruction process.

I would also like to thank the New Zealand Brain Research Institute team for their advice, feedback and awesome lunch time stories. Also would like to thank the team for their work on recruiting and assessing participants. I would like to thank Kyla Wood, for explaining the neuropsycological assessment process, which made understanding the diagnostics criteria much more clearer. I would like to thank Sam, for proof reading my thesis and being support during my writing process.

Lastly, I would like to thank my family and friends, for there support, encouragement and love.

Contents

List of Figures

List of Tables

List of Abbreviations

FBB	**F**lorbetaben
PD	**P**arkinson's **D**isease
PD-N	**P**arkinson's **D**isease **N**ormal Cognition
PD-MCI	**P**arkinson's **D**isease **M**ild **C**ognition **I**mpairment
PD-MCI	**P**arkinson's **D**isease **D**ementia
PDDRS	**P**arkinson's **D**isease **D**ementia **R**isk **S**core
PET	**P**ositron **E**mission **T**omography
PCA	**P**rincipal **C**omponent **A**nalysis
PC	**P**rincipal **C**omponent
PIB	**11C P**ittsburg **C**ompound **B**
ROI	**R**egion **O**f **I**nterest
RF	**R**adio **F**requency
SPM	**S**tatistical **P**arametric **M**apping
SPGR	**S**poiled **G**radient **R**ecalled **E**cho
MNI	**M**ontreal **N**eurological **I**nstitue
MoCA	**Mo**ntreal **C**ognitive **A**ssessment
TOF	**T**ime **O**f **F**light
TOFAC	**T**ime **O**f **F**light **A**ttenuation **C**orrection
TOFNAC	**T**ime **O**f **F**light **N**o **A**ttenuation **C**orrection
ICA	**I**ndependent **C**omponenet **A**nalysis
SUVR	**S**tandard **U**ptake **V**alue **R**atio
WMH	**W**hite **M**atter **H**yperintensity
UPDRS	**U**nified**P**arkinson's**D**isease**R**ating**S**cale
TE	**E**cho **T**ime
TR	**R**epetition **T**ime

TI	**T**ime of **I**nversion
FLAIR	**F**lluid **A**ttenuation **I**nversion **R**ecovery

Chapter 1

Introduction

Parkinson's disease (PD) is a progressive neurodegenerative disease. It is the second most common neurodegenrative disorder after Alzheimer's disease (AD)(Aarsland, Brønnick, & Fladby, 2011). It is defined by the loss of neurons in the brain, specifically the dopamine neurons in the substantia nigra par compacta which lies above the brain stem (Samii, Nutt, & Ransom, 2004)(Braak et al., 2003). Dopamine is a neurotransmitter that plays an important role in allowing normal movements (Braak et al., 2003)(Aarsland et al., 2011). PD is traditionally defined by its motor symptoms, which were initially defined by James Parkinson, and include resting tremors, rigidity, bradykinesia, hypokinesia, akinesia and postural abnormalities (Thomas & Beal, 2007). However, PD is also associated with non-motor related symptoms such as cognitive impairment, dementia, mood disorder, psychosis, sleep disturbance, autonomic dysfunction and alterations in reward, motivation and mood (Chaudhuri, Tolosa, Schapira, & Poewe, 2014). Historically, the survival rate of PD individuals was very low (due to the motor symptoms); hence, the non-motor symptoms were not immediately apparent. Over time, with improvements in treatment and general medical care, non-motor features became more apparent, especially in elderly PD patients.

PD is expected to impose social and economic hindrance on society as the population ages (Pringsheim, Jette, Frolkis, & Steeves, 2014). The prevalence of PD is about 160 per 100,000 and the incidence of PD is about 20 per 100,000 populations (Alves, Forsaa, Pedersen, Gjerstad, & Larsen, 2008). In New Zealand and other developed countries, PD affects about 1% of the population over 65 years of age (Aarsland et al., 2011)(de Lau

& Breteler, 2006). It is more common in those over the age of 65 years. The demographic trend projects that the current estimated prevalence of PD in New Zealand is 10,000 New Zealanders, will increase two-fold by 2035 and four-fold by 2050 (Bach, Ziegler, Deuschl, Dodel, & Doblhammer-Reiter, 2011). PD prevalence varies across-cultures due to difference in environmental exposure and genetic factors. Studies have shown prevalence of PD is higher in males than in females and is also associated with the aging process (Alves et al., 2008)(Pringsheim et al., 2014). More importantly, PD can reduce life expectancy and lead to significant disability and impaired quality of life.

Dementia is 1.7 – 5.9 times more likely in PD patients than in healthy individuals (Factor & Weiner, 2007). The cumulative prevalence of dementia in PD is approximately 75-90 % (Aarsland & Kurz, 2010). Dementia develops due to the progression of degeneration and the deposition of Lewy bodies in the cerebral cortex and limbic structures (Madhavi, 2014). Many demographic and clinical features have been associated with dementia in Parkinson's patients such as older age and motor impairment. These features are Parkinsonism, age, mild cognitive impairment (MCI), neuropsychiatric symptoms and genetic factors. However, studies have been unable to predict the onset of dementia after PD diagnosis, since it is highly variable and can occur anywhere from 2-20 years (Aarsland & Kurz, 2010). After diagnosis, this variability provides a therapeutic window. The ability to identify patients with a higher risk of developing dementia will lead to more effective treatment choice, timing and development.

β-Amyloid is most commonly known as a pathological hallmark for AD (discussed in detail in section 1.1.4) (Gertz & Rajkumar, 2010). However, it has now been recognized as a significant contributor to cognitive impairment in PD. Amyloid deposition in AD is a robust finding and predictive of individuals that will go on to developing dementia. This shows that quantification of the amyloid plaque burden may play a critical role in predicting which individuals are at a 'higher risk' of developing dementia and this could eventually help in the treatment and disease management of PD. Neuroimaging with Positron Emission Tomography (PET) and advanced Magnetic Resonance Imaging (MRI) has shown to be a useful biomarker for providing pathological information in

cases of AD. Recent studies have demonstrated the importance and usefulness of amyloid PET imaging as a tool for diagnosis and understanding the progression of MCI in AD and PD (Gomperts, Locascio, & Rentz, 2013). The first PET ligand to be used as a biomarker for amyloid-beta in AD was 11C-Pittsburgh Compound B (PIB) (Potecorvo & Mintun, 2011). Along with PIB, many other studies have looked at other radiopharmaceuticals as a potential amyloid label, such as Florine-18 radiotracers (Potecorvo & Mintun, 2011). In AD these radiotracers have been a useful tool in diagnosing the early stages of disease in patients that are cognitively normal or have mild cognitive impairment. Clinical trials of anti-amyloid therapeutic intervention are ongoing therefore adequate quantification and location of β-amyloid is essential.

This thesis, will investigate the potential of FBB-PET imaging in PD-MCI subject in order to identify individuals with a higher risk of developing dementia in the near future. In order to do so, it will look at amyloid burden in PD-MCI patients using the FBB-PET imaging. It will further look at understanding the pathophysiology of cognitive decline and dementia. In particular look at how amyloid burden effects the progression of cognitive decline. It determining the association of amyloid accumulation with the cognitive decline in PD-MCI subjects.

The thesis is composed of five chapters, each of them dealing with different aspects of this study.

Chapter 1 introduces and defines basic terminology and reviews literature useful in the context for this thesis. It is subdivided into three parts. Part one describes Parkinson's disease and explains the pathology and problems associated with the disease. Part two describes the neuroimaging used in imaging amyloid deposition in neurodegenrative disorders and it explains the basic concepts of these imaging techniques and discusses previous literature on amyloid imaging using these techniques. Chapter 2 describes and justifies the study design and data gathering method used. It also outlines the method of analyses used i this study. Chapter 3 addresses the results from the data analysis. Chapter 4 discusses the results we acquired, limitations and future work. Chapter 5 summaries the findings of this thesis.

1.1 Parkinson's Disease

1.1.1 Cognitive Impairment in Parkinson's Disease

Cognition is defined as the brain's ability to acquire knowledge and understand through thought, experience and the senses. This unique ability of the brain is affected by many factors such as normal aging and mental health. However, it is severely affected in individuals who are suffering from a neurodegenerative disorder. The degree of cognitive impairment ranges from being mild (mild cognitive impairment) to highly severe (dementia) and varies with the progression of disease generally worsening as the disease progresses (Yarnall, Rochester, & Burn, 2013). At the onset of the disease even non-demented patients are found to have some degree of cognitive impairment (Yarnall et al., 2013). Many studies have shown that the global disability level between PD-normal cognition (PD-N), PD-mild cognitive impairment (PD-MCI) and PD Dementia (PDD) increases in a step-wise manner (Yarnall et al., 2013).

Following the Movement Disorder Task Force Criteria, cognition is divided into five domains (Litvan, Goldman, I.Troster, et al., 2012). The five cognitive domains that could potentially be affected are: learning and memory (ability to learn, remember and acquire new information), attention and speed of processing (ability to focus and understand the task at hand in a timely manner), executive function (problem solving, planning and performing), visuospatial functions (manipulate and understand non-verbal information) and language (ability to understand, use and manipulate language) (Fernandez, Crucian, Okun, Price, & Bowers, 2005a)

Cognitive impairment is one of the defining features of AD. However, it is now also seen as a major issue in other neurodegenerative disorders including PD. In the past 30 years, studies have analysed and investigated in detail the epidemiology of cognitive decline and dementia in PD. It is clear that cognitive deterioration is a common, progressive and disabling factor in PD. Although the majority of PD patients are affected by cognitive decline, the specific deficits can vary between individuals.

1.1.2 Mild Cognitive Impairment

Mild Cognitive Impairment (MCI) was initially seen as a symptom of AD. However, it is now well-established that individuals with PD also exhibit PD-MCI prior to the development of dementia and that cognitive decline is also one of the main symptoms of PD. The frequency of MCI in PD ranges anywhere from 21-62%, with an average prevalence of around 15-18 % for individuals aged 70 years (Goldman & Litvan, 2011)(Madhavi, 2014).

PD-MCI is now recognized as an appropriate stage to address the underlying pathogenic process leading to dementia. It is known as the intermediate stage of impairment from normal cognition to dementia; defined as two impairments at -1.5 standard deviation below the normative data in any of the five task force cognitive domains (discussed in detail in section 2.2) (Palavra, Naismith, & Lewis, 2013) (Dalrymple-Alford et al., 2011a). In PD-MCI, daily life activities are generally unaffected or are only slightly affected. Neuropathology of PD-MCI is heterogeneous, showing deposition of neocortical Lewy bodies, cortical amyloid, Tau, tissue loss and neurotransmitter dysfunction (Compta et al., 2011) (Jellinger, 2010a).

PD-MCI is diagnosed on the basis of neuropsychological testing. These neuropsychological batteries asses individuals and allocate them into certain groups: PD-N, PD-MCI and PDD. For example Litvan et.al., Diagnosis criteria for MCI in PD; movement disorder society task force guidelines, allow characterization of the clinical syndrome and diagnostic methods (Litvan, Goldman, I.Troster, et al., 2012). It is designed using the MDS task force criteria addressing the specific issue of PD. It is divided into four criteria for the diagnosis of PD-MCI: Inclusion criteria, Exclusion criteria, Specific guidelines for PD-MCI level 1 and level 11 categories and Subtype classification for PD-MCI. The inclusion criteria is an initial diagnosis for PD using the UK PD brain bank criteria and PD-MCI is characterized as an informative decline in cognition abilities. The exclusion criteria is used to assess for PDD using the MDS task force (Dalrymple-Alford et al., 2011b). The specific guidelines for PD-MCI level 1 and level 2 are the abbreviated assessment and comprehensive assessment respectively, for the specific diagnosis for

PD-MCI. Lastly, the subtype classification for PD-MCI is important in exploring the impairments in specific cognitive domains. It also classifies PD-MCI into two categories : single and multiple domain. The single domain is defined by the presence of two abnormal test in a single cognitive domain with other domains unimpaired. The multiple domain is defined as one abnormal test in at least two or more cognitive domains. Even with the criteria and guidelines for diagnosis of MCI, it is still challenging because it can not be generalized to all patients, since an individual's mental level of functioning can have a huge influence on their performance on neuropsychological measures (Litvan, Goldman, I.Troster, et al., 2012).

1.1.3 Dementia

Dementia is defined as a syndrome resulting in multiple-domain cognitive impairment severe enough to impair daily life (Quinn, 2014). The general difference between dementia and MCI is the impact of the syndrome on an individual's daily functioning. Dementia has a significant effect on an individual's everyday functions (Fernandez et al., 2005a). It was first introduced by Alois Alzheimer, while describing what came to be known as AD. According to the epidemiological reports since 2010, about 35.7 million people worldwide have been affected by dementia (Quinn, 2014). For many years, AD has been seen as the main cause of dementia. However, many other neurological disorders and medical conditions can lead to dementia over time, for example PD, Lewy Body disease, vascular insult, human immunodeficiency virus, Huntington's disease, Pick disease, depression, hypothyroidism and vitamin B12 deficiency (Quinn, 2014) (Mendez & Cummings, 2003).

In PD, recent studies have shown that the cumulative prevalence of dementia is around 75-90% (MA.Hely, Reid, Adena, Halliday, & Morris, 2008). The incidence of dementia is fourfold higher in PD cases in comparison to the general normal aging population. The effects of dementia on individual daily activities have a huge impact on the quality of life of an individual, public health services and cost of care. The pathological association of dementia in PD is classified into three main categories : subcortical pathology,

limbic or cortical Lewy bodies type degeneration and AD type pathology (Emre, 2003) (Quinn, 2014).

Recently, much effort has been placed on diagnosis criteria designed to distinguish different types of dementia (Emre et al., 2013). Clinical diagnostic criteria used for PDD is similar to PD-MCI. However, in the case of dementia there must be impairment in 2 cognitive domains, along with decline in an individual's everyday activities not including the motor impairments (Dalrymple-Alford et al., 2011b) (Fernandez, Crucian, Okun, Price, & Bowers, 2005b). Many individuals with PD-MCI will develop PDD, but the time of dementia onset varies wildly from patient to patient, ranging anywhere from 2-20 years after diagnosis. Previous longitudinal studies investigating the conversion of PD-MCI transition to dementia have found that about 62% of PD-MCI patients converted to dementia in comparison to 20% of PD patient with normal cognition (PD-N) (Palavra et al., 2013). Therefore, it is important to understand PD-MCI and the pathology driving transition to dementia. This could provide greater prognostic accuracy and more targeted intervention.

1.1.4 Amyloid

Amyloid accumulation has been associated with pathology of many neurodegenerative disorders such as AD, PD, Lewy body disease and Huntington's disease. In PD, amyloid accumulation is a likely contributor to development of Dementia.

β-Amyloid is generated from sequential amyloid precursor protein (APP) proteolysis. APP is a type 1 transmembrane glycoprotein, present at high levels in the brain. It belongs to a family of amyloid precursor-like proteins (APLP-1 and APLP-2). The fundamental role of APP is unknown and is a topic of intense research (Pearson & Peers, 2006). Many studies suggest that APP poses neurotropic properties. The high level of APP plays an important role in neuronal growth, cellular survival and neuronal migration, shown by Oh et al. who looked at the effect of wild-type APP in transgenic mice and found enlargement of neurons and epitomized effects in these mice. Additionally, in a recent study, Young-Pearse et al. demonstrated that APP favors cognitive function and synaptic density improvement (del C. Cárdenas-Aguayo et al., 2014).

In APP processing, there is two pathways. In the non-amyloidogenic pathway, soluble extracellular fragments sAPP- α, are released by cleavage of APP by α -secretase. In the presence of γ-secretase at the plasma membrane, sAPP- α is further cleaved to form APP intracellular C-terminal domains. The second pathway is the amyloidogenic pathway in which the N-Terminal soluble extracellular fragments, sAPP- β and CT99 are released by cleavage of APP by β -secretase. These fragments are further cleaved by γ-secretase to form amyloid-beta (Aβ) fragments (as shown in figure 1.1) (del C. Cárdenas-Aguayo et al., 2014)(Selkoe, 2004) (Vallabhajosula, 2011). The Aβ fragments aggregate to form the amyloid-beta plaque that accumulates in the brain during neurodegeneration.

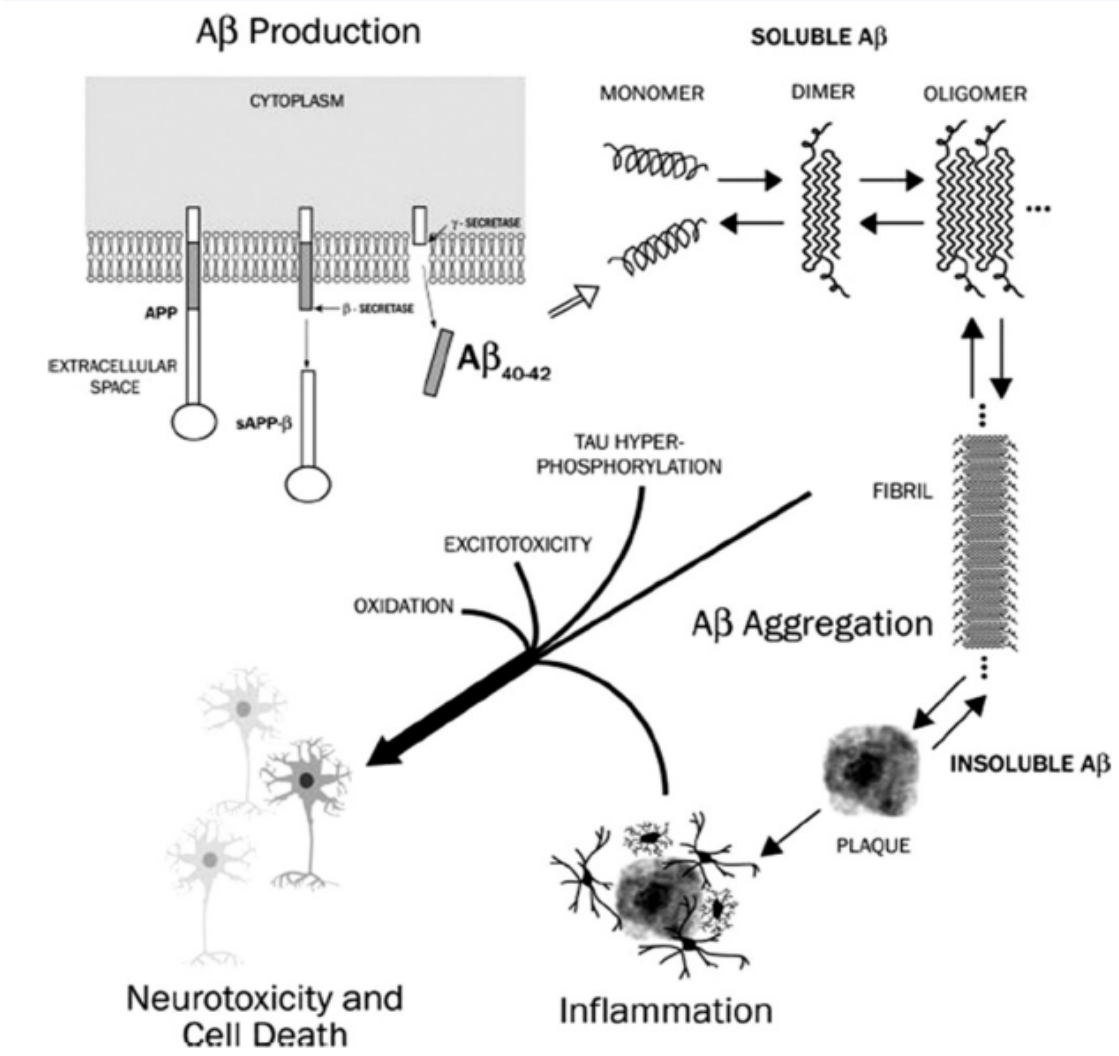

FIGURE 1.1: Schematic diagram of β-Amyloid peptide formation from cleavage of APP by β- secretase and γ-secretase. (Vallabhajosula, 2011)

In the healthy brain, amyloid-beta aggregates are presented in low levels during synaptic activity. Studies have shown the capability of amyloid-beta to function as a chelator and antioxidant when presented at low levels (del C. Cárdenas-Aguayo et al., 2014), with the ability to capture redox metals such as Cu, Fe and Zn. Furthermore, low physiological levels of Aβ favours learning and memory processes and regulates synaptic plasticity (del C. Cárdenas-Aguayo et al., 2014). However, mutation in APP can lead to enhanced levels of generation of the Aβ aggregates which have been linked to neurodegenerative disorders, neurotoxicity and cell death. In the case of PD, amyloid plaque accumulation is linked to potential decline in cognitive function and ultimately to PDD pathology. Studies have demonstrated the contribution of accumulation of β-Amyloid in the progression of cognitive decline in individuals with PD and other neurodegenerative disorders (Gomperts et al., 2013). It has been shown that 50% of PDD patients undergo secondary diagnosis of AD. Neuroimaging of β-Amyloid in case of AD has shown to be a useful tool in providing pathological information. However, in the case of PD and PDD, previous imaging data has generally shown no difference. Few studies, in previous years have shown association between amyloid deposition and cognition or future dementia in PD (Gomperts et al., 2013). We want to see whether β-Amyloid deposition adds an additional 'hit' to PD-MCI, which pushes them to convert to PDD. We also want ti investigate whether we can see an association between β-amyloid and cognition in PD.

1.2 Medical Imaging

1.2.1 Positron Emission Tomography (PET)

Fundamental Principles of operation

Positron emission was first discovered in 1933 by Thibaud and Joliot. The objective of PET scanning is to measure the concentration of distribution of radionuclide in the living body. The radionuclides used in PET imaging have one principle property beta

plus (positron) decay . It is this positron decay that is employed in PET imaging in order to acquire PET images. The most common positron-emitting isotopes used in PET imaging are carbon-11, Oxygen-15, Nitrogen-13 and Fluorine-18 (Ziegler, 2005). These isotopes are produced using a Cyclotron (charged particle accelerator) (Bushberg, Seibert, Leidholdt, & Boone, 2002). It bombards stable nuclei with high energy to generate radioactive isotopes. These isotopes have two things in common. Firstly, their nuclei are rich in protons which means that in order to stabilize themselves, they convert the excess proton into a neutron and release a positron and neutrino. Secondly, they have relatively short half-lives, enabling an adequate trade-off between image quality and minimal radiation dose. These isotopes are distributed in the subject with the help of carrier molecules (biological substrate). The biological substrate used and tagged to the isotope depends on there specific function in the body. The most common biological substrates used in PET imaging are glucose, H2O, CO2 and O2 (E.Schmitz, Alessio, & Kinaham, 2003). The isotopes are tagged to a specific carrier molecule chemically to create a specific radionuclide that will bind to a specific target (Bushberg et al., 2002).

These radionuclides are then injected into the bloodstream and undergo positron decay. During positron decay of the radionuclide, a proton converts into a neutron, resulting in the release of a positron with specific kinetic energy Q, as shown in equation 1.1 (Basu, Kwee, Surti, Akin, & Yoo, 2011).

$$Z^{A}\mathrm{X} \rightarrow Z - 1^{A}\mathrm{Y} + \beta + \nu + Q \tag{1.1}$$

A positron is an antimatter equivalent of an electron and it annihilates with an electron. So when a positron is released, it travels a certain distance and then annihilates with a nearby electron, losing its kinetic energy (Basu et al., 2011). The range that the positron travels depends on the positron's energy and the characteristics of the tissue (density and the atomic number). The annihilation leads to the conversion of electron and positron into collinear emission of two 511 KeV photons (Bushberg et al., 2002). Due to the collinear emission of the photons, the photons emitted travel in opposite directions to one another in a straight line (known as the Line of Response (LOR)),

shown in figure 1.3. The emission of two photons ensures the conservation of linear momentum and energy (Basu et al., 2011).

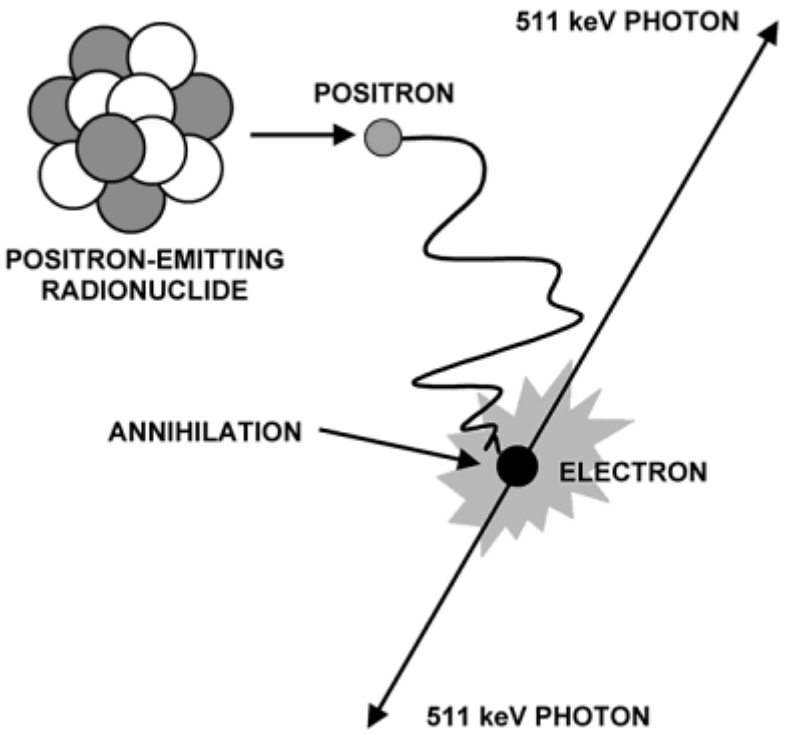

FIGURE 1.2: General principle of PET imaging : Release of positron, annihilation with electron and production of two 511 KeV annihilation photons.(Phelps, 2006)

The two annihilated photons in the opposite direction are detected simultaneously by the detectors surrounding the patient, allowing localization of the origin of these photons. This mechanism is known as the annihilation coincidence detection. The detectors are arranged in an array surrounding the patient in a circular fashion (Bushberg et al., 2002) (Basu et al., 2011). There are three possible annihilation coincidence event types detected by PET detectors. These events are: true coincidence (two photons from a single annihilation event are recorded within a specific coincidence time window of 6 - 15 nanosecond (Cherry, Sorenson, & Phelps, 2003)), Accidental coincidence (random coincidence-two single photons from two unrelated annihilation events reach the

detector in the coincidence time window and the event is registered as a single coincidence event) and Scattered coincidence (event due to Compton scattering in the patient body).

Both the scattering and accidental coincidence detection lead to incorrect LOR and results in incorrect positional information, loss of contrast, hazy background and noise in the PET image. These coincidences are the main source of inaccuracy in clinical PET scanning and so correction for these is important, to acquire fine detail and useful information from PET scans(Cherry et al., 2003).

Data Acquisition and image formation in PET imaging

Photon detection and scintillator detector

For coincidence detection, the detectors in the PET scanner are arranged in a circular fashion. They are made up of a scintillator crystal such as sodium iodide doped with thallium (NaI (TI)) and bismuth germinate (BGO), Lutetium oxyorthisilicate (LSO), coupled with a photomultiplier tube (PMT) in a block design (Cherry et al., 2003). A matrix of scintillator crystals is attached to 4 PMTs arranged in 2X2 matrix. The matrix is achieved by segmenting the crystal into smaller elements. The block detector allows the small scintillator crystal to be used to improve spatial resolution while keeping the number of PMT as low as possible to control the cost. The scintillator crystal uses the concept of light distribution and centroid calculation in four PMT to identify in which element the gamma ray was detected from. The choice of scintillator used in the detector depends on the stopping power of the detector for 511KeV photon, the effective atomic number of the scintillator crystal, the scintillator decay time, the light output per KeV of photon energy, and the energy resolution of the detector (E.Schmitz et al., 2003). These parameters are important as they determine the spatial, energy and timing resolution of the system and the efficiency of the detector in detecting true coincidences (Farncombe & Iniewski, 2013).

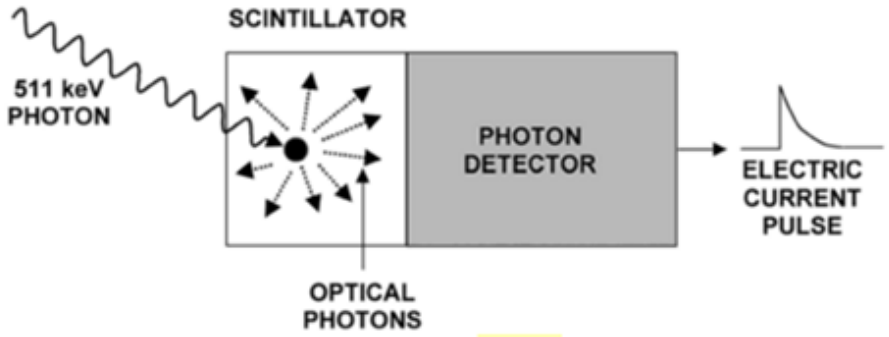

FIGURE 1.3: Scheme of a Scintillator Block Detector. Fundamental principle of scintillator block detector.(Phelps, 2006)

In principle, the scintillator crystal interacts with the gamma rays and the energy from the gamma rays is converted to light. 511 KeV annihilation photons create tens of thousands of visible wavelength photons in the scintillation process. The light energy from the crystal is passed on to the PMT, which produces pulses of electrical signal. A PMT tube is a vacuum glass tube which consists of a photocathode that converts the light energy into photoelectrons, which are then passed on to dynodes. The dynodes multiply the photoelectrons depending on the voltage difference between the dynodes and the photocathode. The amplified photoelectrons are passed onto the anode which in turn convert the photoelectrons into an electrical pulse signal (Casey & Nutt, 2007).

Data processing and correction

One of the most important techniques performed to correct and eliminate detection of unwanted coincidences, and also determine the origin of true coincidence is Time of Flight (TOF). Time of Flight is applied to improve the single to noise ratio (SNR) in the image and also helps reduce the random coincidence detection (Basu et al., 2011). The concept of Time of Flight (TOF) in PET image reconstruction is based on measuring the precise time that each of the coincident photons are detected at, for each of the annihilation coincidence events. The majority of PET scanners acquire coincidence event pairs which lie in the time window of 6-15 nanoseconds (Cherry et al., 2003). However, these scanner do not record the time of arrival of these photons. As mentioned earlier,

a scattering coincidence can be detected if it lies between this time window. This could result in the wrong location of the coincidence event and leads to noise in the reconstructed image. To acquire images with Time of Flight correction, the detector must have a short light decay times which is accomplished by using LSO or LYSO scintillator crystals (Basu et al., 2011). In the TOF technique, the arrival time of every event is recorded . If the event is detected between the time window of 0.5 nanoseconds then the time difference $\Delta\tau$ is calculated and computed (Cherry et al., 2003) (Farncombe & Iniewski, 2013). Using the time difference, the location of the annihilation event is calculated (equation 1.2).

$$d = \frac{\Delta\tau c}{2} \tag{1.2}$$

Where d is the location of annihilation event and with the center of the gantry as the midpoint, c is the velocity of the light (3 x 10-9 cm/sec). To acquire information about the events and the image, the probability of line of response (LOR) is recorded, which represents the location of the annihilation event. This allows the LOR to be shorter than the LOR from detector to detector. Due to the shorter time window of 0.5 nanoseconds, the detection of random and scattered coincidences is minimized (Rich & Christian, 2013).

Once all the lines of coincidence are observed and recorded by the detector as shown in figure 1.4, they are organized in a sinogram (raw data format). In the sinogram, each sinusoidal curve represents all the lines of coincidence passing through a single point in the subject. The sinogram is further modified to acquire only information in the form of true coincidence events and eliminates attenuated information and information obtained by the scattered and random coincidence events (E.Schmitz et al., 2003).

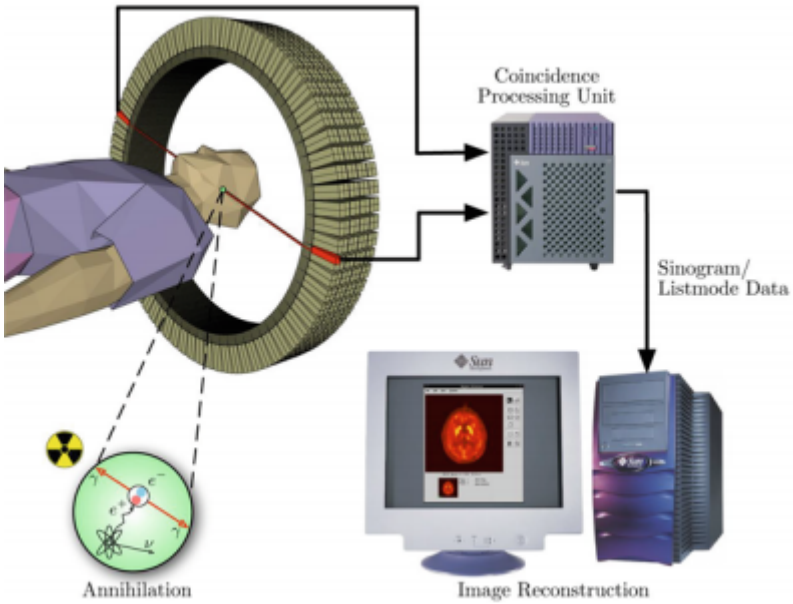

FIGURE 1.4: Schematic representation of the Image Acquisition and Reconstruction in CT/PET imaging System. (Striet, 2010)

Another important correction done in PET imaging is attenuation correction (Kinahan, Hasegawa, & Beyer, 2003). The emission of radiation from the radionuclide inside the body is not always observed by the detector due to two factors: absorption of radiation within the body and the scattering of photons away from the detector. This loss of detection of true coincidence is known as attenuation. In PET brain imaging, half of the true coincidence is lost due to attenuation.

In PET imaging, attenuation of photons is characterized by the linear attenuation coefficient (μ). The linear attenuation coefficient is the transmission probability of the photon through any material. Attenuation depends upon the thickness of the body, atomic number and density (Ay & Sarkar, 2003). It can affect the visual quality of the PET images (image noise, image artifacts and image distortion) and in turn affect the quantitative information of PET data (Ay & Sarkar, 2003). The probability of the the coincidence acquired by the detector depends on the linear attenuation coefficient of the tissue at 511 KeV and the total length of intersection within the body (T), as illustrated below in equation (1.3).

$$P(det) = e^{-\mu T} \tag{1.3}$$

Where P(det) is the probability of detection (Cherry et al., 2003).

The probability of detection is independent of the location of the source, and only depends on the length of the LOR. Attenuation correction is performed by generating attenuation maps, which represent the spatial distribution of the linear attenuation coefficient of 511 KeV photon. There are two ways the attenuation map can be generated in PET imaging: by the transmission method and the transmission-based method (E.Schmitz et al., 2003).

In clinical application, the most common and effective method used is the transmission-based method. In transmission-based method, an external source is used, such as a CT scan. In our study, we have used this CT-based attenuation correction method in acquiring PET images corrected for attenuation. Here CT information is used to generate attenuation maps (E.Schmitz et al., 2003). A tomographic reconstruction algorithm is used to calculate the attenuation coefficient at the applied voltage energy. The attenuation coefficient is further converted to an attenuation coefficient at 511 KeV energy, to allow correction for the 511 KeV photon emission in the PET scan. Using CT-based attenuation correction allows higher photon fluence rates, faster transmission scan along with a true anatomical structural image and true capability of locating the radionuclide, which is not achieved in a normal transmission scan (E.Schmitz et al., 2003).

Applying the CT image to the PET image also overcomes a limitation of PET imaging namely, the lack of an anatomical reference frame; thereby providing the specificity of the examination in neuroimaging. For example, in most clinical cases, the PET (functional) image will be co-registered to the CT (structural) image (E.Schmitz et al., 2003).

Clinical PET scanners now routinely use the Iterative Reconstruction method (Iniewski, 2009). This reconstruction method, along with attenuation correction, allows for three dimensional image representing the distribution of the radionuclide in the body. Iterative reconstruction methods solve the system of linear equations to acquire projection

data from an initial image, by converting the image into pixels or voxels (volume elements or pixels) (Iniewski, 2009) (Cherry et al., 2003). It relates the image pixel and projections using a linear equation system which can be represented as below:

$$P = AX \tag{1.4}$$

where P is the array of projections, X is array of image pixels and A is the coefficient matrix of the system. The matrix A, consists of the weighted factor contribution from the image pixel to the projections (Zeng, 2010).

Iterative Reconstruction initially estimates a uniform distribution of activity (image). Using forward projection, it sums all the intensities in the projection data of the estimated image. The summed estimated projection data is then compared with the actually recorded projection data, in order to acquire a close approximation to the recorded projection data. This is achieved by finding the difference between the estimated and the recorded projection data and back projecting the error projection on to the estimated image. This process is repeated until the difference between the actual data and the projected data is minimized as shown in figure 1.5. Lastly, the images are smoothed to eliminate noise (Iniewski, 2009) (Cherry et al., 2003).

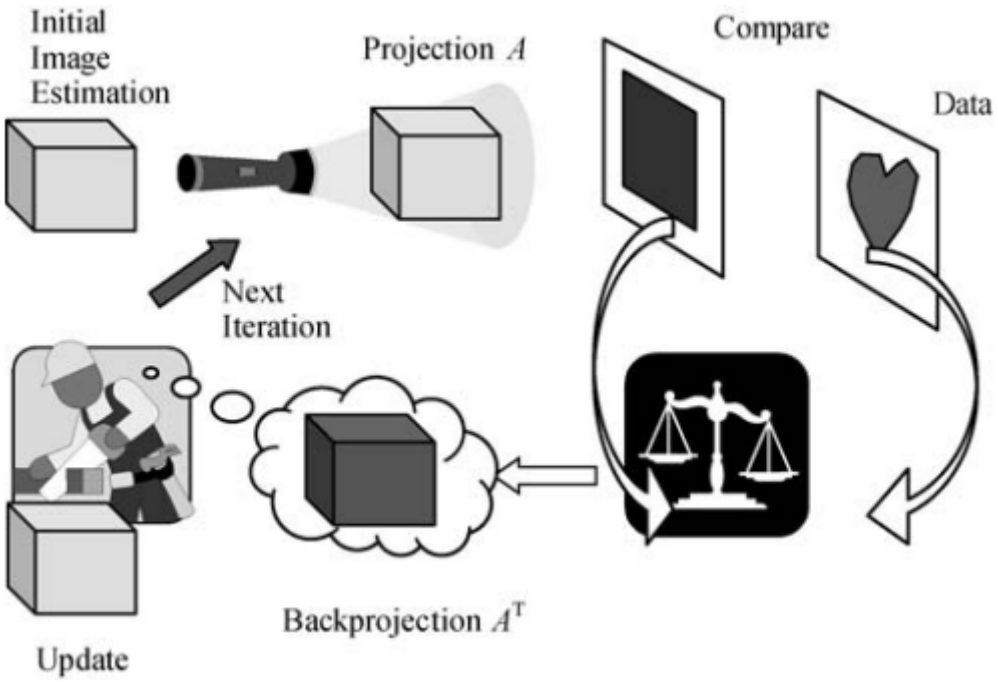

FIGURE 1.5: Basic schematic representation of principle of Iterative Reconstruction Algorithm (Iniewski, 2009)

The high sensitivity, specificity and accuracy of these reconstructed images make PET images a useful tool for the clinical diagnosis of certain disease. Due to this unique quality of PET imaging, it makes it an ideal tool to employ to understand amyloid accumulation in PD-MCI.

In order to evaluate the PET images, abnormal tissue radiotracer uptake relative to the normal tissue is determined (Standard Uptake Value Ratio). Standard Uptake Value Ratio (SUVR) is a method of acquiring the concentration of radioactivity in the PET imaging. It is sometime referred to a the differential uptake ratio (DUR). In this thesis we will refer to it as SUVR. It is obtained by measuring the concentration of radioactivity in the region of interest on a PET image, normalised for the injected dose and body weight of an individual (Saha, 2015).

Amyloid PET Imaging

Amyloid has been a hot topic in neurological research for the past ten years, particularly in AD. The development of in-vivo amyloid PET imaging has provided a breakthrough in clinical neuroscience. The amount of amyloid accumulation can now be measured before autopsy. In AD, Amyloid PET imaging has been used to show increase deposition relative to healthy aging, and is one of the most robust findings. Presence of amyloid is even predictive of future development of dementia in those with MCI (Gomperts et al., 2013). It has been used in PD studies to evaluate the association of amyloid aggregation with PD symptoms and its pathology in PD. Many studies using amyloid imaging have shown amyloid accumulation in PD with significant spatial distribution in comparison to AD (Campbell et al., 2013). Pathological studies, say that up to 50% of PDD cases have amyloid accumulation that results in a secondary diagnosis of AD (at autopsy) (Jellinger, 2010b) (Compta et al., 2011). In the field of PD, one of the interesting questions many researchers are interested in is the story of amyloid in PD and how it is associated with cognition in PD (Gomperts et al., 2013).

The first attempt at imaging amyloid in-vivo was performed by Friedland and colleagues (Friedland et al., 1997). They used the radiotracer technetium-99 linked to an amyloid antibody fragment in AD patients using single-photon emission tomography (SPECT). This was an unsuccessful attempt since the fragment was unable to effectively cross the blood brain barrier (Friedland et al., 1997). However, it started the interest in developing and investigating the potential of amyloid binding radiotracers which will efficiently allow amyloid imaging. Since then, the possibility of imaging amyloid has increased due to the development of specific tracers for PET that bind efficiently to amyloid plaques (Potecorvo & Mintun, 2011). The tracers belong to a variety of chemical classes such as thioflavin T, stilbenes, benzoxazoles and benzofurans. These tracers are 18-fluoro-labelled 1,1 dicyano-2-[6-(dimethylamino)-2-naphthalenyl] propene (FDDNP), 11 C-labelled [N-methyl]-2-[4- methylaminophenyl-6 hydroxybenzothiazole](Pittsburgh Compound-B, PIB), 18F-florbetapir ((E)-4-2(6(2(2(2[18F] fluoroethoxy)

ethoxy) ethoxy) pyridin-3-yl) vinyl)-N-methylbenzenamine) and 18F-florbetaben [trans-4-(N-methyl-amino)-4 (2(2(2[18-F]fluoro-ethoxy) ethoxy) ethoxy) stilbene](FBB) and many more (Richards & Sabbagh, 2014).

Florbetaben (FBB) is one of a handful of new 18-F-Labeled tracers produce for β-Amyloid imaging in humans. It is synthesized in a similar fashion to other F-18 tracers. A non-radioactive precursor is labelled to 18-F, which undergoes acid hydrolysis and chromatography for purification. In terms of toxicity, FBB is found to be under the tolerance limit with no mutagenic properties. It was demonstrated that a quantitative measurement and a visual interpretation can be made with a 20min PET scan, following a 90 minutes post-injection period (Richards & Sabbagh, 2014).

Preclinical and post-mortem AD studies have shown that the binding affinity and density of FBB to Aβ aggregates is in the range required for bioimaging. On average, the binding affinity for Fluorine-18 tracers is around 6.7 nM and does not show any binding to Lewy bodies, Pick bodies or glial cytoplasmic inclusions (Richards & Sabbagh, 2014). As a diagnosis tool for early AD, it has been proven to be cost effective and provides improved quality of life to the patient. This finding was provided by Guo and colleagues, who investigated the impact of FBB on diagnostic confidence and economic implications (Guo et al., 2012). They designed a model which allowed exploratory analysis using payer and society perspectives, along with the course of disease and the time of diagnosis. They showed that using FBB PET as a diagnosis tool in AD improves quality of life for a patient by providing faster diagnosis compared to other diagnosis tools and has a positive impact on economic output (Guo et al., 2012).

PIB was the first amyloid PET tracer and is the most studied amyloid-binding radiotracer. It was first used in 2003 in AD mice models to show amyloid deposition as a hallmark of AD. It showed rapid entry in the brain and efficient binding to amyloid aggregates; specifically to extracellular and intravascular fibrillar amyloid-beta deposition, without binding to neurofibrillary tangles or Lewy bodies. Correlations between PIB and amyloid aggregates have been well documented in AD cases. AD PET studies have shown association between PIB binding and the cognitive decline, in the early stages of AD. Edison and colleagues showed that uptake of C-11 PIB in AD revealed

an increase in β-amyloid in the areas associated with cognition deterioration (cingulate, frontal, temporal, parietal and occipital cortical area) (Gomperts et al., 2013). Another C-11-PIB PET study associated with amyloid deposition in AD reported a two-fold increase in PIB uptake in the cortical area in cases of AD, in compared controls. Amyloid PET is also informative in early AD and even MCI, where by amyloid positive MCI individuals are at higher risk of developing dementia than those with a negative amyloid PET scan. PIB has been used in many other studies to investigate the amyloid deposition association with PD, PDD and other neurological disorders. Recently, PIB amyloid deposition has been associated with the rate of cognitive decline in PD. Gompert et.al reported an increase in cognitive decline in PD individuals with low levels of cortical amyloid deposition in comparison to individuals with amyloid free cortical area (Gomperts et al., 2012). This finding has given us the push to further look into understanding the amyloid association in PD .

These studies have shown the high efficiency and accuracy for indicating amyloid accumulation in the brain and have shown the high sensitivity of PIB as a diagnostic marker in AD. However, PIB-C11 radiotracer has its limitations as it is unable to be used as a clinical application, due to its short half-life of 20 minutes. To overcome this limitation, other PET ligands have been developed and investigated, such as F-18 labelled tracers. Since F-18 tracers have a longer half-life of 110 minutes, they allow regional distribution and clinical applications.

Villemagne et.al and others have shown the high accuracy and efficiency of FBB for indicating amyloid accumulation in the brain and that it provides robust separation between AD and healthy controls (Villemagne et al., 2012).

Degree of retention of FBB is lower than PIB. This means the dynamic standard uptake value ratio of FBB is narrower. However, in the same study it was observed that both tracers had high retention in the cortical grey matter and lower uptake in white matter in those with AD. The ratio of frontal cortex to white matter ratio for PIB was 1.45 for AD subjects (Villemagne et al., 2012).

Barthel and colleagues showed that the sensitivity and specificity of FBB is 80% and 91% respectively to distinguish AD subjects from a healthy control group (Barthel et

al., 2011).

1.2.2 Magnetic Resonance Imaging

Magnetic Resonance Imaging (MRI) is a non-invasive technique which provides high quality anatomical and functional images for a range of tissue types in the human body. The MR system consists of: the superconducting magnet, radiofrequency coils and gradient coils. Generally, the magnet used in MRI is a superconducting magnet (1.5 Tesla or higher) and is used to generate a strong constant magnetic field. The radiofrequency coil is made up of a transmit coil and a receiver coil. The transmit coil produces the radiofrequency pulses (discussed in detail later in this section) and the receiver coil detects the MR signals. The gradient coils produce small variations in the magnetic field and allow localization of the image slice (Bushberg et al., 2002).

MRI principle of operation

The basic principles of MRI are based on the magnetic properties of the nucleus of the hydrogen atom. Every atom has a property known as spin (Bushberg et al., 2002). The hydrogen atom is the most abundant nucleus in the human body, due to water and fat content. MRI uses these hydrogen atoms and its property of spin (Bushberg et al., 2002). Due to spin, the hydrogen atoms produce a magnetic moment vector μ and act as little magnets with weak magnetic fields (Mikla & Mikla, 2013). In nature, these magnetic moment vectors are orientated at random.

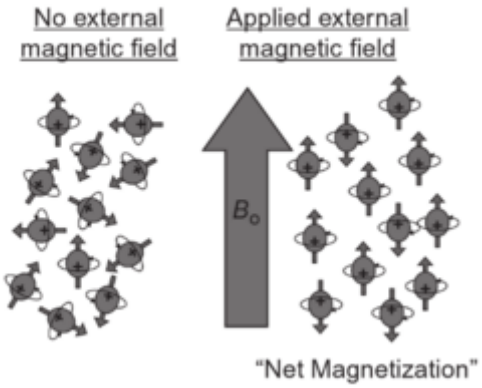

FIGURE 1.6: Orientation of hydrogen atom in nature (absence of external Magnetic Field) and in the presence of an external Magnetic field. In the absence of magnetic field the hydrogen atoms are orientated at random and the net magnetization is zero. In the presence of external Magnetic field, the atom orientate in two direction: parallel to the magnetic field or anti-parallel to the magnetic field (as depicted by the direction of the small arrows portraying the atom axis of spin) (Mikla & Mikla, 2013)

MRI manipulates these hydrogen atoms and their magnetic moment vector by using an external magnetic field, in order to produce a net magnetization as shown in figure 1.6 (Mikla & Mikla, 2013). More precisely, when a magnetic field is applied in the MRI system, the protons experience torque which causes the magnetic moment vector to align with the magnetic field (Brown & Semelka, 2011). This also results in precession of these vectors around the external magnetic field. There are two orientations in which the protons align themselves in the presence of an external magnetic field: parallel (spin-up) or anti-parallel (spin-down). The spin-up orientation is a low energy state whereas the spin-down orientation is a higher energy state and so the majority of the proton nuclei prefer to align themselves in the parallel orientation. More protons in the spin-up orientation result in a net difference in the orientation of proton alignment and this difference creates a net magnetization vector, parallel to the external magnetic field (Brown & Semelka, 2011) (Mikla & Mikla, 2013).

The frequency of proton precession around the magnetic field is governed by the Larmor frequency w. The Larmor frequency depends on the strength of the external magnetic field (B) and the gyromagetic ratio γ of the tissue (equation 1.5) (Bushberg et al., 2002).

$$w = \gamma B \tag{1.5}$$

In MRI, in order to acquire MR signals, the net magnetization (M) is manipulated by applying a pulse of radio-frequency energy (RF pulse) at the resonant frequency of the proton, perpendicular to the external magnetic field. The RF pulse is known as the excitation pulse. This pulse allows the protons to absorb energy at a given frequency and then re-emit energy at the same frequency. For an efficient MRI system, this pulse is tuned to the Larmor frequency (processional frequency of the protons), resulting in changing the energy levels of protons (Brown & Semelka, 2010). The proton absorbs the RF energy and move from a lower energy state (parallel to the magnetic field) to a higher energy state (anti-parallel to the magnetic field). The number of protons that undergo this change depends on the RF pulse amplitude and duration, which ultimately determines the net magnetization orientation (Weishaupt, Köchli, & Marincek, 2006)(Brown & Semelka, 2010).

In terms of macro-level, the net magnetization can be described on Cartesian coordinate axis system (xyz plane). Initially the net magnetization is in the z axis which is parallel to the applied magnetic field (B). This is due to a greater number of protons in the lower energy state than the higher energy state. As the RF pulse is applied, with the right amplitude, duration and resonant frequency, the net magnetization can be excited and rotated to any desired angle (flip angle). For example, by applying the RF pulse perpendicular to the external magnetic field, with a high enough amplitude and certain duration, it will result in the net magnetization (initially in the direction of the external magnetic field) rotating to the transverse plane (x-y plane). Initially, immediately after the RF pulse is applied, all the nuclei spins are in phase in the transverse plane. When the RF pulse is removed, three processes take place simultaneously. Firstly, the RF energy absorbed by the proton is re-emitted at the resonance frequency. Secondly, the

excited protons return to their original equilibrium position (z-plane orientation) by the process known as T1 relaxation (spin-lattice or longitudinal relaxation). Thirdly, in the x-y plane, the in-phase net magnetization (exited proton) begin to dephase, by the process of T2 relaxation (spin-spin or transverse relaxation). The emission of the electromagnetic energy during the relaxation processes is eventually detected by a detector in a MR scanner (Bushberg et al., 2002).

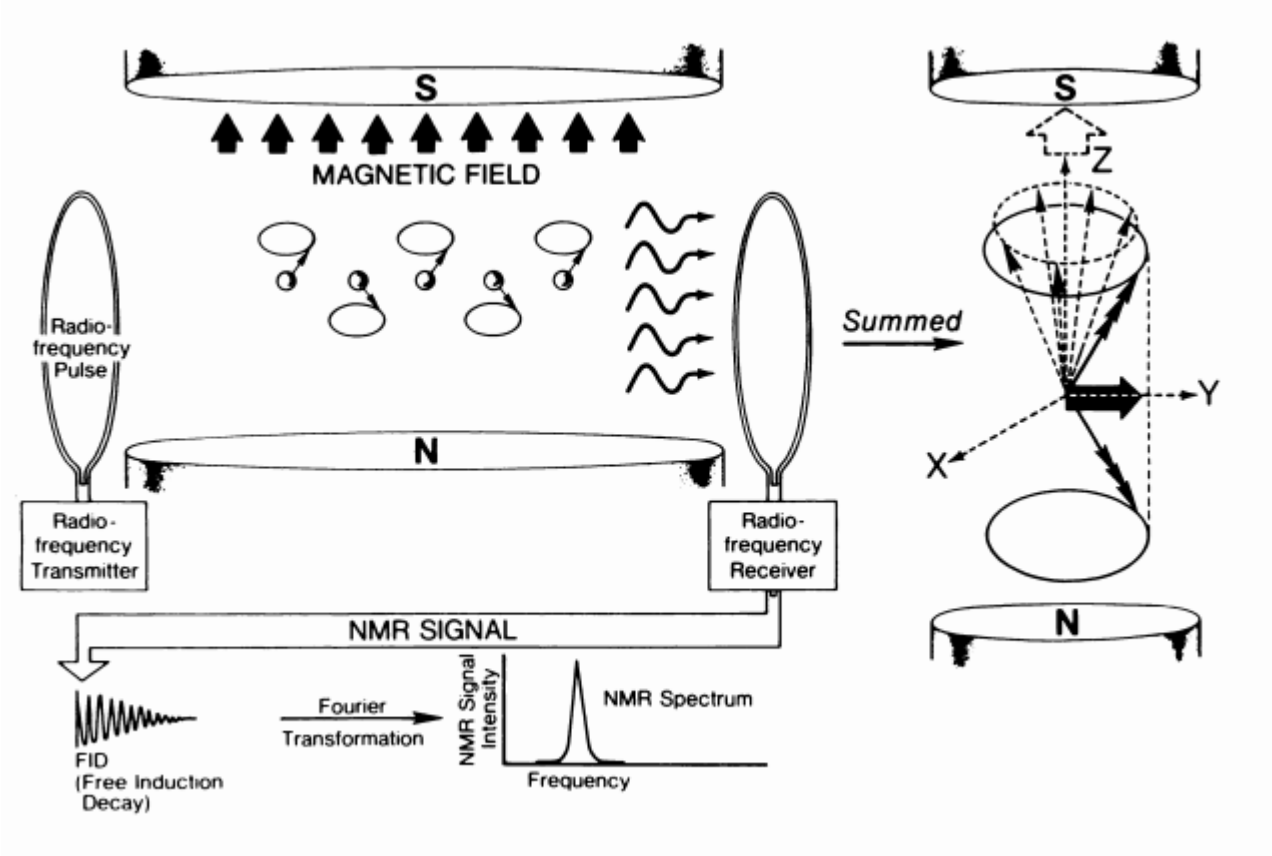

FIGURE 1.7: Manipulation of net Magnetization by applying a RF pulse. The intensity of the MR signal received depends on the amplitude of the RF pulse, the duration of the RF pulse and the Larmor frequency.(Harms et al., 1984)

The T2 relaxation measures the energy transferred from one excited proton to another nearby proton. During T2 relaxation, dephasing of the xy magnetization takes place. This change in the magnetization induces an electromotive signal in the RF receiver coil. This sinusoidal electrical signal is known as the free induction decay (FID) signal. The FID signal depends on the amplitude of the net magnetization before the RF pulse

is applied and the relaxation time. The amplitude of the FID signal decreases over time in an exponential manner (eq. 1.6) (Bushberg et al., 2002).

$$M(t) = Mo(e^{-t/T2}) \tag{1.6}$$

As mentioned earlier, T1 relaxation process takes place simultaneously with T2 relaxation. During this process, the z magnetization return to the equilibrium in an exponential manner (eq: 1.7) (Bushberg et al., 2002). T1 relaxation time measures the rate of energy transferred from the excited nuclei to the environment (lattice), hence the name spin-lattice relaxation (Bushberg et al., 2002) (Brown & Semelka, 2011).

$$M(t) = Mo(1 - e^{-t/T1}) \tag{1.7}$$

The relaxation times T1 and T2 are different for different tissues; this allows the MR system to identify different tissue based on their magnetic properties. In other words, these relaxation mechanisms determine image contrast (Bitar, Leung, Perng, & Roberts, 2006). Tissues with longer relaxation times appear different to those with shorter relaxation time. For example, fat has a shorter T1 recovery time (recovery faster) and a shorter T2 decay time (decays faster) in comparison to water, which has a longer T1 recovery time and T2 decay time. It is this recovery rate of signal that enables MRI to differentiate between different tissue types and acquire clinical images (Bitar et al., 2006) (Bushberg et al., 2002).

Data Acquisition and Image Formation in MRI system

To acquire an MR image, a pulse sequence is used, which is the timing and strength of radiofrequency and gradient pulses used to determine the contrast of the image. The FID signal is acquired indirectly by creating "echoes", or when a decaying signal is refocused. In MRI, echoes can be generated in two ways, either by using a 180° (spin echo) or by reversing the gradient polarity (gradient echo). In order to create echoes, both of these methods rephase the spins which were initially dephasing after the net

magnetization was rotated into the transverse plane. Once all the spins are in phase in the transverse plane, an echo signal is generated. This echo signal is collected by the detector in the MR scanner and is used to form an MR image.

A pulse sequence is basically a wave form with various magnetic gradients and RF pulses. There are two fundamental types of pulse sequence: Spin echo (SE) and gradient echo (GE). The other various pulse sequences are derived from these pulse sequences by adding different parameters to these pulse sequences to create images such as T1 weighted image, T2 weighted, proton density and Fluid attenuation inversion recovery (FLAIR) images. Different applications require different anatomical or functional information and image contrast. To achieve this, certain parameters are manipulated in a pulse sequence. These parameters include: repetition time (TR), Echo time (TE), Time of inversion (TI), RF pulse flip angle and gradients (Bitar et al., 2006) (McRobbie, Moore, Groves, & Prince, 2007).

A basic pulse sequence requires a certain sequence of events in order to acquire signals. In a basic pulse sequence, there are four sets of events which take place in order to acquire an MR image. Firstly, a RF pulse is applied as shown by the top line in figure 1.9. At the same time, a slice selection gradient is applied in the z plane (second line in figure 1.9). This is followed by a phase encoding gradient in the direction orthogonal (y axis) to the slice selection gradient. The phase encoding allows encoding of the phase of the MRI signal. Lastly, a frequency encoding gradient is applied in the x axis during the decay of the echo; acquiring all the frequency information in the MR signal. Simultaneous to the frequency encoding, data sampling and acquisition of the complex signal take place (Bitar et al., 2006) (McRobbie et al., 2007).

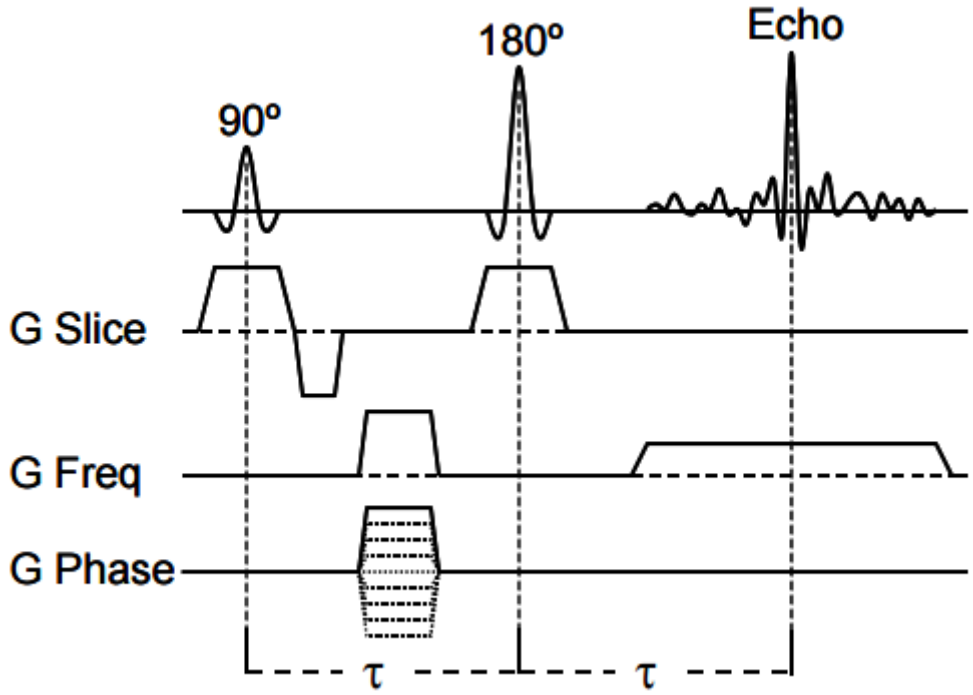

FIGURE 1.8: schematic of basic events in a SE pulse sequence. Initially, an excitation pulse is applied, followed by switching on and off gradients (slice selection, phase encoding and frequency encoding); followed by an inversion pulse to produce an echo (blue pulse) and finally signal readout.(Hahn, 1950)

This data sampling and acquisition takes place using a one-dimensional Fourier transform. The Fourier transform converts the signal into discrete frequency values and corresponding amplitudes. It stores this information in a k-space matrix. The k-space matrix is a two-dimensional matrix with positive and negative spatial frequency values. In the matrix, the x-direction represents the frequency encoded variables and the y direction represents the phase encoded variables. Once the entire k space matrix is filled, inverse Fourier transform in applied. It decodes the frequency domain variation into a spatial domain (image) (Bushberg et al., 2002) (McRobbie et al., 2007).

Spoiled Gradient Recalled Echo Imaging

In this study, anatomical MR imaging was only used as the base for processing prior to the statistical analysis. In this section we will focus on the gradient echo pulse sequence as we used a T1- weighted spoiled gradient recalled echo (SPGR) image (Bushberg et

al., 2002). A SPGR image provides a high resolution anatomical image which is in close proximity to the tissue macroscopic image. It uses a gradient echo pulse sequence in order to eliminate the transverse magnetization before applying the second RF pulse (Hashemi, Bradley, & Lisanti, 2012). Since it eliminates the transverse magnetization by using a shorter TE, it minimizes the T2 characteristics of the tissue. So SPGR obtain image contrast by manipulating the TR and the flip angle. It uses shorter TR to minimize the recovery of the longitudinal magnetization, thereby enhancing the T1 relaxation characteristic of different tissues. Also, shorter TR allows faster image acquisition and maximizes signal to noise ratio in the image (Hendrick, 2007).

T2 Weighted Fluid Attenuation Inversion Recovery

T2 weighted Fluid attenuation inversion recovery (FLAIR) imaging is a unique imaging pulse sequence which produce a strong T2 weighted image with suppressed fluid signal (Bushberg et al., 2002). This pulse sequence is most commonly used in neurological imaging to exclude non-disease related pathology and to enhance signals from periventricular lesions (Brant-Zawadzki, Atkinson, Detrick, Bradley, & Scidmore, 1996). It uses conventional Spin Echo pulse sequence with a 180° inversion pulse and a prolonged T1 recovery time. The longitudinal magnetization recovery time is set to the time it takes for the cerebrospinal fluid (CSF) longitudinal magnetization to reach zero crossing point. This will allow removing of the signal from CSF from the resultant image (Brant-Zawadzki et al., 1996).

1.3 Image Preprocessing

Image preprocessing is a vital step in any medical imaging application. It is important to minimize noise and sampling errors. The steps performed in image preprocessing (discussed in detail in chapter 2) aim to process the data so that it is suitable to be analysed statistically. In this study, image preprocessing was performed using statistical parametric mapping (SPM, University College London) software ($http://www.fil.ion.ucl.ac.uk/spm/$).

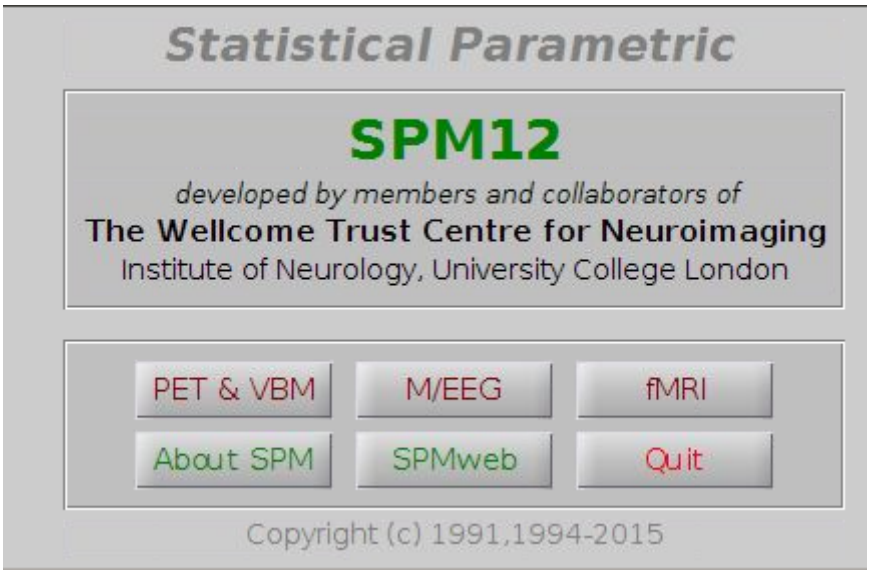

FIGURE 1.9: Statistical Parametric Mapping 12

SPM is designed to facilitate image preprocessing and voxel-based analysis of structure, function and disease-related changes in the brain (Friston, Ashburner, Kiebel, E.Nichols, & Penny, 2011). Image preprocessing using SPM is discussed in detail in chapter2.

Chapter 2

Methodology

2.1 General Information

Fifty subjects with PD-MCI were either recruited from a local specialist movement disorder clinic or were volunteers from an ongoing longitudinal PD study at the New Zealand Brain Research Institute. The demographic and clinical characteristics of the participants are described in Table 2.1.

TABLE 2.1: Summary of demographic and clinical characteristic

	Mean(SD)	Range
Age(years)	73(6)	59-86
FBB dose (MBq)	300(17)	240-346
Clinical Characteristic		
Hoehn and Yahr stage	2.56(0.56)	1.5-4
PD duration (years)	6.9(4.9)	1-20
UPDRS motor score	40.92(13.54)	13-68
Cognitive indices		
MoCa score	21.78(3.67)	12-28
Attenuation Z score	-1.02(0.76)	(-3)-(0.53)
Executive Function score	-1.14(0.74)	(-2.64)-(0.72)
Learning Z Score	-0.93(0.90)	(-2.42)-(1.54)
Language Z score	-0.52(0.68)	(-2.56)-(0.64)
Visuospatial functional Z score	-0.80(0.84)	(-2.54)-(1.02)
Global Cognitive function Z score	-0.98(0.64)	(-2.44)-(0.62)
WAIS-III information subtest score	107(10)	86-125
PD dementia Risk Score	0.65(0.3)	0.04-0.99

The diagnosis of PD was performed using the UK Parkinson's society criteria. Recruited individuals had motor symptoms at least a year prior to study entry, to exclude dementia with Lewy body cases. All subjects received a clinical evaluation, structural

MR imaging and FBB PET imaging, along with cognitive assessments. Exclusion criteria included prior neurosurgery for PD and medical conditions such as stroke, head injury and learning disabilities. All subjects gave written consent. The study was also approved by the Upper South Regional Ethics Committee of the New Zealand Ministry of Health.

2.2 Neuropsychological Assessments

The neuropsychological assessment employed in this study was designed and performed by members of the New Zealand Brain Research Institute (NZBRI). The assessment, which takes anywhere from 2.5 - 5 hours to complete, is routinely used in the assessment of patients cognition at the NZBRI. In this study, the NP battery was performed to ensure that the subjects fulfilled the diagnostic criteria for PD-MCI; with the different neuropsychological test scores also being obtained for statistical analysis.

The neuropsychological assessment was conducted in two sessions and it examines five cognitive domains posed by the Motor Disorder Society-Task Force Level-II requirement for PD-MCI (Litvan, Goldman, Tröster, et al., 2012). These four domains were: executive function, attention/working memory, learning memory, language and visuospatial/visuoperceptual skills. These domains were individually assessed using different assessments. Executive function was assessed by examining the Stroop interference, letter fluency, category fluency, category switching, action fluency and trails. Attention and working memory were examined by testing everyday attention, Stroop colour reading, Stroop word reading, digits forwards/backwards and digit ordering. The learning and memory domain were assessed using California verbal language test-II short form (short and long delays) and the Rey complex figure test (short and long delay). The visuoperceptual performance was measured using judgment of line orientation, fragmented letters, the picture completion test and Rey complex figure copy. Lastly, language was assessed using the Boston naming test, dementia rating scale-2 similarities sub-test and the Alzheimer's Dementia assessment cognitive scale (Wood et al., 2016).

The scores obtained for these sessions were used in categorizing the participants according to their cognitive statues (PD-N, PD-MCI and PDD) and to acquire a summary of global cognitive ability,'Global cognitive Z score' (discussed in more detail later in this section). The categorizing was done using the MDS Task force criteria for MCI (Litvan, Goldman, Tröster, et al., 2012)(-1.5 standard deviation (SD) below the normative data on at least two tests within one of the four domains) (Dalrymple-Alford et al., 2011b) and PDD dementia assessment which incorporates an evaluation of everyday function. MCI criteria required the individual had unimpaired daily functional activities but met the operationalized criterion of impairment of 1.5 standard deviation or below the normative data in at least two of the five MDS cognitive domain assessments. From these scores a global cognitive Z score was obtained by averaging the score from the MDS cognitive domains excluding the language domain scores (Litvan, Goldman, Tröster, et al., 2012).

2.3 Magnetic Resonance Imaging

All subjects underwent an MRI scan. The scan was conducted using a 3T GE HDxt MR scanner with an eight channel head coil, at Hagley Radiology. The 3T Magnetic field scanner provides stronger signals, enables high quality images to be acquired at a faster rate, with high resolution and good contrast. The structural T1-weighted images were obtained for image preprocessing of the PET images and T2 Flair images were obtained to quantify white matter hypertensity volumes.

2.3.1 Scanning protocol

The structural MR images were acquired using a T1-weighted, three dimensional spoiled gradient echo (SPGR) acquisition with following parameters: TE = 2.8ms,TR = 6.6ms, TI = 400ms, flip angle = 15°, acquisition matrix = 256 x 256 x 170, Field of View (FOV) = 250mm, slice thickness = 1mm, voxel size = 0.98 X 0.98 X 1.0mm^3, scan time = 5 min and 6 sec.

T2 Flair images were acquired with the following parameters: TE = 104.5 msec, TR = 9000 msec,TI = 2250 ms, Flip angle = 90°, reconstruction matrix = 512 x 512 x 32, FoV = 220 mm, slice thickness = 3 mm, and scan time = 2 min 56 sec.

2.4 Positron Emission Tomography

All the subjects were scanned using a GE discovery 690 PET scanner at Southern Cross hospital. Subjects were injected with 300 MBq of F18- Flurobetaban (FBB), prepared at Cyclotek Ply Ltd (the major supplier of PET radio-pharmaceuticals) in Melbourne, Australia. It was ensured that the radioactive exposure of FBB to the patient was under the recommended radiation exposure of 300 $\pm$ 20% MBq and the tracer dose was under 55 μg per injection. Prior to the PET scan, a computer tomography transmission scan was obtained for each individual to perform attenuation correction by the PET/CT scanner. Time of flight and attenuation correction was applied by the scanner during image reconstruction at the time of scanning. Time of flight was obtained using the iterative Time of Flight plus the SharpIR algorithm. SharpIR is an iterative reconstruction method employed by general electric (GE) company to reconstruct PET images (Ross & Stearnsr, 2016).

During image reconstruction, two types of images were obtained: Time of Flight with Attenuation Correction image (TOFAC) and Time of Flight with No Attenuation Correction (TOFNAC). The purpose of obtaining these images is discussed in detail in section 2.5.2.

All the subjects were placed in the scanner with head pads and neck support to ensure that the patients would be comfortable and that their head would be kept still for 20 minutes (duration of the scan). The CT was acquired first (to facilitate attenuation correction). The PET acquisition was obtained 90 minutes post injection of FBB, with an acquisition time of 20 min. For the CT, the direction of the scan was caudocranial with 120 kV and 30 mA. The PET and CT images were reconstructed with the following parameters: Slice thickness of 3.75 mm; Slice interval of 3.27mm; Field of View (FoV) of 50cm; Pitch of 0.969:1 and Rotation time of 0.5 second. In order to acquire TOFAC

images during the reconstruction process, the SharpIR algorithm was applied, with a reconstruction resolution of 3 mm full width half maximum (FWHM); 16 subsets and 4 iterations. For TOFNAC images all the parameters were kept the same except no attenuation correction was applied.

2.5 Image Preprocessing

Image preprocessing is a vital step in any medical imaging application, prior to any statistical analysis. It enhances the visual appearance of images and transforms the raw data into a version which is easier to work with and perform statistical analysis on.

In this study, it was used to remove noise, correct for artefacts and eliminate patient motion. It also ensured that the brains of all participants were registered, i.e. each voxel in the image corresponds to the same region in the brain of each individual. This allows accurate group analyses by normalising each individual brain image into a standard space.

In this study, image preprocessing was performed by using Statistical Parametric Mapping (SPM12) (Welcome Department of Cognitive Neurology, University College London,UK) in MATLAB versions 7.4 (R2014a, Mathworks, Massachusetts, USA).

Initially, all the images (MR and PET) were converted from their original file format Digital Imaging and Communications in Medicine (DICOM) into single Neuroimaging Informatics Technology Initiative (NifTI) format files, since SPM operates on NifTI format files (Friston et al., 2011).

2.5.1 Magnetic Resonance Image Preprocessing

The preprocessing of structural images included bias correction, normalisation of the structural images, tissue classification and removal of non-brain tissue. Using SPM 12 allowed us to perform these steps using a single model, developed in 2005 by Ashburner and Friston, known as the Unified segmentation (AshburnerT & Friston, 2005).

Using this model, T1-weighed SPGR images were tissue classified. This partitions the structural image into voxels containing grey matter, white matter, cerebrospinal fluid (CSF) and skull using tissue probability maps (TPM), as shown in Figure 2.1.. Then combines dartal normalisation and bias correction with tissue classification.

FIGURE 2.1: Segmentation of structural image into A. Grey matter; B. White matter and C. Cerebrospinal fluid

Before using these prepossessed structural images for further image preprocessing, segmented volumes were visually inspected to ensure that they were accurate and contain no gross errors. In order to acquire, white matter hyperintensity (WMH) lesion volumes, the lesion segmentation toolbox, 20 was employed. This toolbox looks for T2 hyperintensities in the T2 FLAIR images and T1-weighted image. This derived a WMH lesion volume for our fifty participants. This WMH lesion volume was used to see an association or interaction of amyloid accumulation with WMH.

2.5.2 Positron Emission Image Preprocessing

The initial step of PET image preprocessing was to eliminate motion effects. Motion artefact in brain imaging is a serious problem in terms of image quality. It is important to minimize motion from the scans for analysis, especially in the case of brain study. From previous studies (associated with amyloid accumulation in PDD and AD), it has been understood that the abnormal amyloid accumulation in PD is in the cortical grey matter of the brain. Any motion present in the scan can cause inaccurate analysis, as the area of interest (cortical grey matter) is only 4 millimetres thick. Furthermore, due

to motion, the signal from the white matter could be mistakenly taken as the signal from the cerebral cortical area.

Even though we try to ensure that there is no head motion during the scans, it is impossible to eliminate head motion from the scan during scanning. This is because our participants have PD with motor symptoms such as tremor at rest. Therefore, in order to acquire a high image quality and accurate analysis of amyloid accumulation in the cortex, motion is eliminated from the images during the image preprocessing step.

In this study, two approaches were taken for motion correction, from which the most effective method was chosen. For both approaches, it was important to reconstruct the single frame of 20 minute dynamic scan into four frames of 5 minute scans. During PET scanning two types of images were taken as discussed in the PET scanning protocol TOFAC and TOFNAC. In the first method, the motion correction was applied prior to attenuation correction, so TOFNAC images were used. In the second method, motion correction was applied after attenuation correction, so TOFAC images for preprocessing were used.

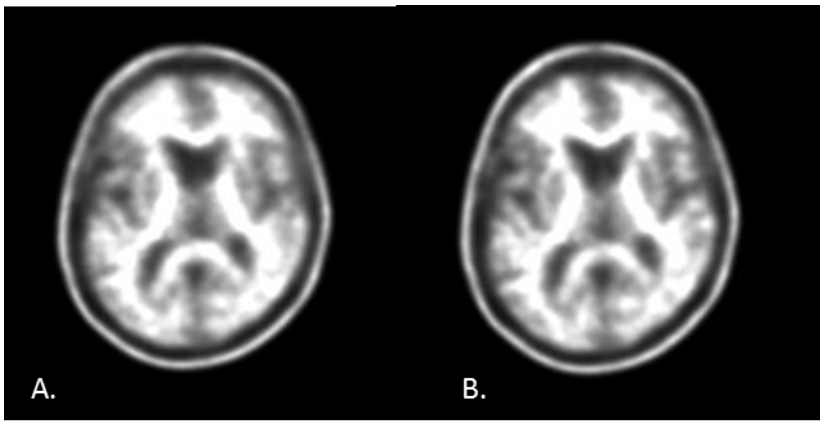

FIGURE 2.2: Motion correction. A. a single frame of 20 minute dynamic scan. B. Realigned and summed image of four frame of 5 minute scans. Note: B has minimised motion which provide much ore clear regional uptake in comparison to A.

We used SPM 12 Realignment and Reslice processing to eliminate motion. The step realigns the volumes to a reference image. Generally, the reference image is the first volume imported in the time series. For example, in our case it took the first 5 minute frame image as the reference image and realigned the remaining three 5 minute frames

to the first frame using a least squares approach and a six parameter rigid body transformation. This reduces motion and increases signal to noise ratio (SNR). During the realignment process, a text file and plots were generated which provide an estimate of the transitional, x-, y- and z- direction ("right", "forward", "up"), and estimated rotation ("pitch","roll","yaw") as in Figure 2.3. For each individual, the plots were examined to make sure that the estimate transition in all three directions was less than 4 millimetres. This method of motion correction can only correct for motion of about 4 millimetres. In this study, any individual with motion greater than 6 millimetres translation or 5 ° was excluded from the study (Friston et al., 2011).

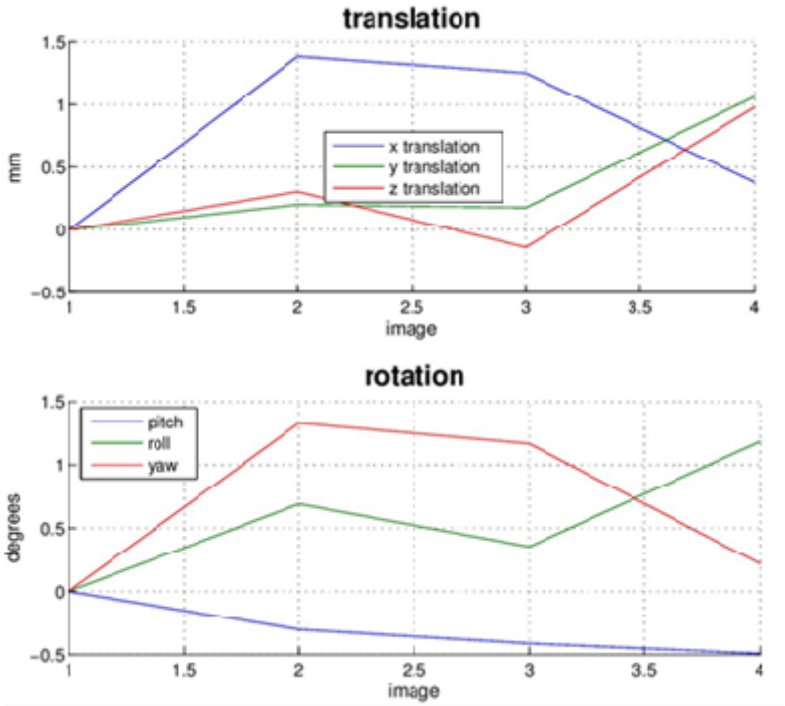

FIGURE 2.3: Realignment and reslicing

Once all four frames were realigned, the images were summed to generate a single frame (Figure 2.2). Once the summation process was over, in the case of the second method, the TOFAC image was ready to be used for further preprocessing. However, in the case of the first method, the TOFNAC images underwent attenuation correction using a MATLAB 7.4 script file (Appendix A). The script file applied attenuation correction to the motion corrected TOFNAC images, by using attenuation coefficient maps and reconstructed an image using the radon transform. Radon transform is a

tomographic reconstruction method that calculates the sum of pixel intensity in each direction (line integral). It maps an image from the Cartesian coordinates to polar coordinates (x', θ) (MathWorks, 2015). One drawback with this method was that by using radon transform, the image quality was reduced (Figure2.4). Due to this reason, the second method was used throughout the study for motion correction. The second method provided excellent image quality and also the desired information for statistical analysis.

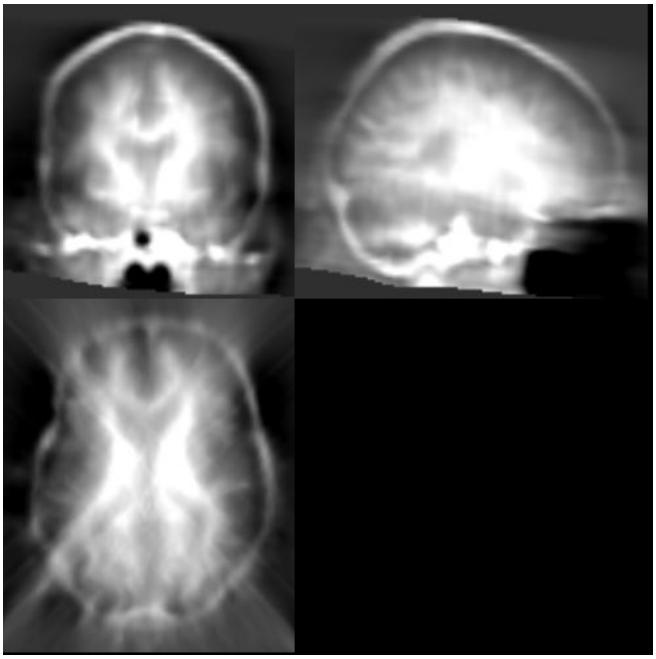

FIGURE 2.4: Attenuation correction of PET motion corrected image using Radon transform.

Once the images had undergone motion correction, they were co-registered to the downsampled structural SPGR images. Since the positioning of the subject during an MR scan and PET scan is slightly different, it is important to co-register the structural image (SPGR MR Image) to the summed functional image (PET image).

Once all the volumes were in the same origin as the structural volumes, all the images underwent Normalisation. Normalisation is a non-linear registration process which spatially transforms the data into a standard space for future analysis. This allows us to reduce variation in brain images from each individual (while maintaining difference of interest) allowing meaningful group comparisons to be performed successfully. Here,

normalisation was conducted in two sets: DARTEL Normalisation and warping the images into standard space.

Diffeomorphic Anatomical Registration through Exponentiated Lie Algebra (DARTEL) Normalisation is a non-linear image registration process which matches individual images to the Montreal Neurological Institute (MNI) template. Templates are pre-existing images to which our individual images are aligned. These templates contain information about the location of the anatomical features in the MNI coordinate space(Friston et al., 2011). DARTEL normalisation creates a template by warping the segmented structural grey matter and white matter images together for each individual (Figure 2.5). This template is used as a deformation field for warping other images which are not in the MNI space but images must be aligned with structure MRI, hence the coregistration of the summed PET image to the structural MRI.

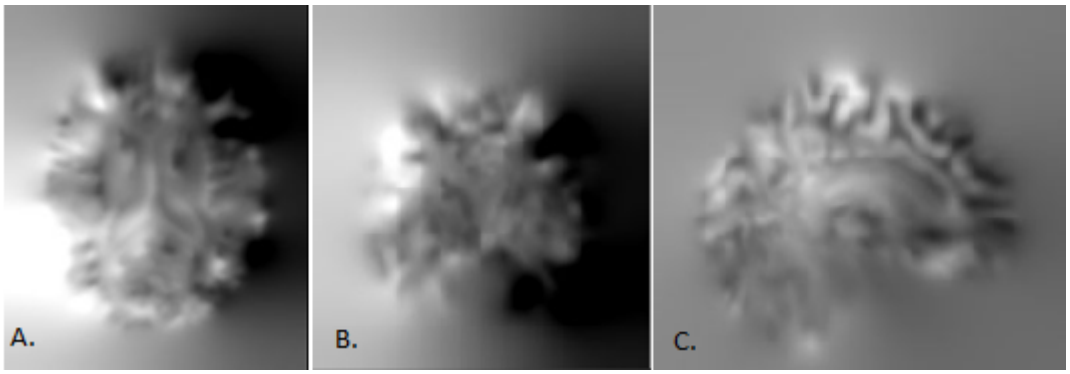

FIGURE 2.5: DARTAL Normalisation from fields, i.e. how a voxel must be warped to align with standard space(defined here as MNI-SPACE).

The second part of normalisation (applying the deformation fields), allows generation of spatially normalised images by warping the non-structural images and segmented images. In this study, the segmented grey matter images and PET images for each individual were normalised using the deformation fields (generated in the first step of normalisation) for each individual. In this step, we modulated the grey matter segmented images and left the PET images unmodulated. The reason the grey matter images were modulated was to compensate for the effect of spatial normalisation. During spatial normalisation, volumetric differences are introduced and this can alter the total amount of signal in the voxel. Modulation to the grey matter images, preserve the

total amount of signal in the normalised segmented images. On the other hand, in the case of the PET images, unmodulation helps preserve the concentration of signal in the volume. Before data analysis was performed, all normalised images were visually examined to ensure that they were accurate and were not grossly mis-aligned.

2.6 Data Analysis

To evaluate the PET images and compare the FBB retention across individuals, a Standard Uptake Value (SUV) was calculated for all voxels. SUV is defined by the concentration of radioactivity in the Region of Interest (ROI) in the PET image, normalised for the injected dose and body weight of an individual (Equation 2.1).

$$SUV = \frac{Concentration}{Injecteddose}(bodyweight) \tag{2.1}$$

In this study, the SUV was calculated using the preprocessed FBB-PET images in standard space (MNI-space). Standard Uptake Value Ratio (SUVR) were acquired using the cerebellar cortex as the reference region. In each individual the cerebellum cortex was defined as the union of the Harvard-oxford cerebellar atlas and the segmented grey matter map (in each individual; Appendix B). The SUV at each voxel was divided by the mean FBB signal in the cerebellar cortex, producing SUVR values at each voxel. These SUVR images were the images analysed in this thesis. They represent the relative accumulation of amyloid in each individual, normalised to uptake in the cerebellar cortex.

2.6.1 Clinical Amyloid Diagnosis

FBB PET images of all the subjects were clinically assessed by a specialist neuroradiologist from Christchurch Radiology Group (Ross J Keenan). The assessment was conducted using the Standard GE healthcare clinical inspection reporting form designed for [18-F]-Flutemetamol PET image. This was performed using COMRAD Radiology

Information System (RIS) which is a comprehensive workflow software. FBB positivity was evaluated in five cortical regions: frontal lobes, posterior cingulate/precuneus, temporal lobes, parietal lobes and striatum. The scans were considered either positive (FBB(+)), equivocal or negative (FBB(-)).

Positivity was based on the amount of signal in the five cortical regions and also the visibility of gyrus, midline (bleeding of signal), precuneus and striatum gap in these regions. A positive FBB image was defined as high accumulation of amyloid in the cortical region of the brain in comparison to the white matter. Whereas, a negative FBB image was defined by no amyloid accumulation in the cortical regions of the brain.

2.6.2 Statistical Analysis

Statistical analysis was performed using the smoothed SUVR images obtained from each subject. The SUVR images were smoothed using an isotropic Gaussian kernel with FWHM of 8 mm. Smoothing suppresses noise and reduces the effects due to residual misalignment. Using the smoothed SUVR images, the uptake ratio for 5 cortical regions of interest (whole cortex, frontal lobes, posterior cingulate/precuneus, temporal lobes, and parietal lobes) and three subcortical regions (striatum, putamen and thalamus) was calculated. These 8 regions were defined by the Harvard-oxford cortical and subcortical probabilistic atlases. In addition, we employed a multivariate analysis of FBB-PET data set to identify a pattern of uptake associated with amyloid deposition. We used linear regression (lm in R studio version 3.0.2) to investigate the association between ROI SUVR and Cog Z (averaging the score from the MDS cognitive domains excluding the language domain scores)/PDDRS (Parkinson's disease dementia "risk" score, predicted the probability of risk that an individual has of converting to dementia in the next 4 years); with age, sex and UPDRS (motor impairment scale) as co-variates. We also checked for a significant group-by-Cog Z/PDDRS interaction, to investigate whether the FBB(+) group behaves similarly to the FBB(-) group. The comparisons were considered significant if $p<0.05$. The two multivariate methods I employed were principal component analysis (PCA) and independent component

analysis (ICA). Lastly, I applied bootstrapping to provide an estimate of the reliability of the identified network.

Principal Component Analysis

Principal Component Analysis (PCA) is a multivariate data analysis technique that has been used in many applications such as face recognition, image compression and finding pattern in large data sets (Rencher & Christensen, 2012). It uses an orthogonal linear transformation technique which transforms the original correlated data set into a new coordinate system which provides information about the variance in the data set (Rencher & Christensen, 2012). It does this by extracting main source of variation in the data set. These variations are expressed as vectors (known as Principal Components or PCs)(Figure 2.6). These projections (PCs) are orthogonal to each other and uncorrelated. These projections highlight the similarities and differences in the high dimension data set. In order to acquire the variance projection data using PCA, initially the mean of the data set is subtracted from the data set (between and within subjects). For example, our data set is represented by Matrix A(m, n) where m is the number of participant and n is the number of voxels (the ID representation of the 3D image). I firstly, subtracted $\bar{m}$ from the m values and $\bar{n}$ from the n values. This results in a matrix of values with a mean of zero (Rencher & Christensen, 2012). This is further used to calculate the covariance matrix as shown in Equation 2.2. The covariance determines how much variation is present in each dimension with respect to the mean of the data set.

$$cov(X, Y) = \frac{\sum_{i=1}^{n}(X_i - \bar{X})(Y_i - \bar{Y})}{n - 1} \tag{2.2}$$

Once the covariance matrix was calculated, the eigenvalues and eigenvectors were determined. The eigenvectors and eigenvalues provide useful information about our data. The eigenvectors corresponds to the principal components and the eigenvalues associated with each eigenvector, yield the fraction of variability explained by each principal component (Rencher & Christensen, 2012).

In matrix form these principal components are expressed as:

$$P = SV \tag{2.3}$$

Where P is the principal components of the original data set (V) and S is the eigenvector matrix, which rotates and stretches the V matrix into P matrix (Stühler & Merhof, n.d.) . Using the scaled eigenvectors (that represent the expression of each principal components in each participant), principal component images were generated. Furthermore, the eigenvectors were transposed to acquire principal components score for each participant (Stühler & Merhof, n.d.).

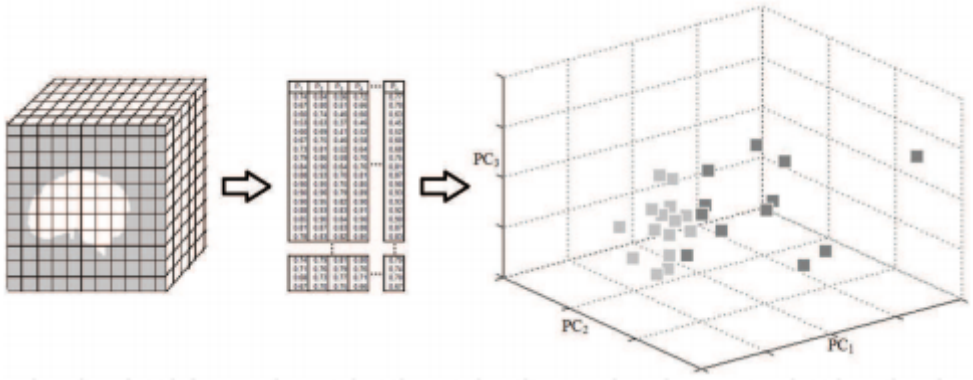

FIGURE 2.6: principal Component Analysis: A. 3D representation of a brain image for a person ; B. Representation of data after transformation of X subject by Y voxels, where each 3D image has been converted into a 1D vector ; C. Example plots of expression of the first 3 PCs i.e. the eigenvalues in each individual associated with each of the eigenvectors,PCs (Stühler & Merhof, n.d.)

One of the advantages of PCA is that it provides the information of the maximum variance in the data set in the first few principal components. So for a large data set such as our where the dimension depends on the number of participants and the number of pixels, PCA makes it easier to interpret and analyse the data. More specifically, the first principal component contains the maximum variance followed by the second component and so on.

PCA has been previously used as a statistical tool in a number of studies associated with neurological disorders, including both PET and MRI studies of PD and AD. In this

study, I employed voxel-based PCA to identify the pattern of variance in FBB deposition, to highlight regions with high amyloid accumulation. Using the PC score, we also looked at the correlations between amyloid accumulation and global cognitive score and neurological test score, along with the visual assessment. After performing PCA, I investigated the first N components that explained more than 66% of the variance. This was done using logistic regression; identifying PCs that were associated with amyloid positivity (as defined by the clinical diagnosis). These PCs were then used to create an amyloid positive network, formed as a linear combination of PCs that significantly contributes to the prediction of amyloid positivity. We then calculated the expression of this amyloid network, the network score and investigated whether this score was associated with global cognitive score, motor impairment(UPDRS3), WM hyperintensity volume, age or sex.

Independent Component Analysis

To see similar or different patterns of amyloid accumulation as seen in PCA, Independent Component Analysis (ICA) is a linear transformation technique (Comon, 1994). However, ICA allows non-Gaussian data analysis so that the components are statistically independent. It is most commonly applied for data compression, Bayesian detection, source localisation and deconvolution (Comon, 1994).

In ICA, the weighting matrix is determined slightly different to PCA, which is represented by the inverse of the matrix S in equation 2.3. Since the components are statistically independent, one component doesn't give any information about another component. This is slightly different than PCA because PCA seeks for components that best represent the data set whereas ICA seeks for components that are most independent from each other. ICA provides independence for non-Gaussian data sets. I performed ICA using The FastICA package (free (GPL) MATLAB program)($http://www.cis.hut.fi/projects/ica/fastica/$) that uses the Hyvarinen's fixed point algorithm (Hyvärinen & Oja, 2000).

ICA has been previously used in studies using functional MRI in AD, looking at alterations in memory networks in MCI (Celone et al., 2006). Similar to PCA, I applied

ICA on our data set to acquire components associated with amyloid accumulation in different regions of the brain. I then used linear regression to determine whether any ICs were associated with Cog score, motor impairment, age or sex.

Bootstrapping

Bootstrapping is a statistical non-parametric technique (Han & Luos, 2014). The purpose of bootstrapping is to estimate the accuracy of a sample statistic. It is virtually impossible to analyse the whole population; instead, we have a sample of the population which may not give a true distribution of the whole population. The validity of our sample set is unknown and the sample set could be biased. To overcome this issue of a biased sample set, we apply bootstrapping. It uses a Monte Carlo method and resamples the data set (as shown by the overview of bootstrapping in figure 2.7)

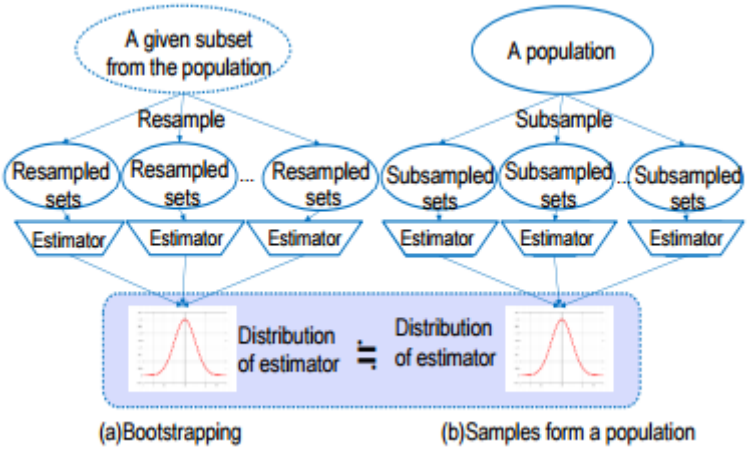

FIGURE 2.7: Overview of Bootstrapping. a. bootstrapping creates specified number of resampled sets with the same size as the subsample from the population while using replacement from the subsample. (Han & Luos, 2014)

It resamples the data with replacement, for a specified number of times, while keeping the sample size the same (in this case the sample size remains 50 participants). Also, it computes the distribution of the estimates to the original sample set. One of the differences between bootstrapping and other resampling methods is that it allows duplication of a participant in a given resampled set. I created a bootstrapped amyloid network for each of the 5000 resampling. This provided an estimate of the

population mean and standard deviation. A z-scored mean was then approximated by dividing the sample network (already determined) by the bootstrapped standard deviation. This image was thresholded at Z = - 1.96 and + 1.96, corresponding to $p < 0.05$ for display purposes.

Chapter 3

Results

3.1 Clinical Amyloid Diagnosis

Of the 50 PD-MCI participants, 9 received a clinical classification of FBB positive, 2 equivocal, and the remaining 39 were clinically amyloid-negative (FBB(+)). These clinical classifications were used in the quantitative analyses. In all further analyses, the 2 equivocal clinical cases were treated as amyloid-positive (FBB(-)).

Figure 3.1 shows an example of a clinically positive FBB scan (left) and a negative scan (right). The negative amyloid scan characteristically showed FBB uptake in deep white matter without any relevant FBB uptake in the cerebellar grey matter. The positive amyloid scan had FBB retention in the neocortex region from the reference region (cerebellum cortex).

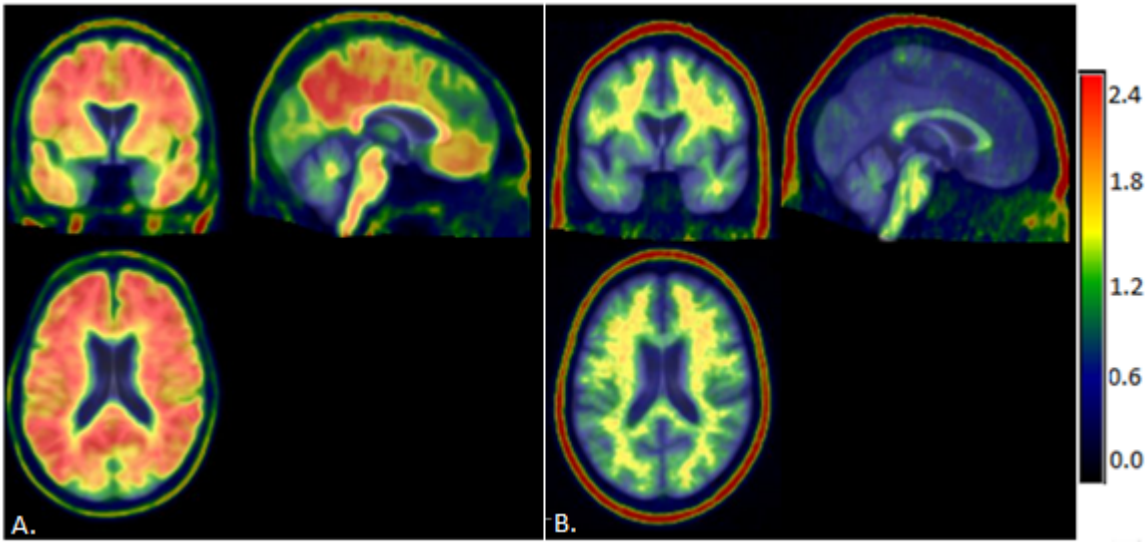

FIGURE 3.1: Example of FBB PET axial, sagittal and coronal images overlaid on the co-registered MR structural image, representing: A. Clinical positive amyloid scan and B. Clinical negative amyloid scan. Colour Bar represent the standard uptake value ratio (cerebellar cortex). The Positive amyloid scan clearly show higher FBB retention in the cortical area of the brain in comparison to the negative amyloid scan. The colour bar also displays the scaling of Standard uptake value ratio (red is high uptake and blue/black is low uptake).

3.2 Regional FBB Retention in PD patients

The mean and range of FBB retention in each region of interest (ROI) is reported in Table 3.1.

TABLE 3.1: Summary of regional FBB SUVRs

	Mean(SD)	Range
Neocortical (global)	1.16(0.19)	0.82 - 1.79
Frontal cortex	1.08(0.24)	0.65 - 1.82
Temporal cortex	1.24(0.25)	0.77-2.06
Posterior Cingulate and Precuneus	1.26(0.29)	0.933 - 2.4
Thalamus	1.10(0.16)	0.71-1.5
Putamen	1.45(0.20)	1.18-2.4
Caudate Nucleus	0.79(0.12)	0.54-1.10

SUVR values were significantly higher for the FBB(+) group relative to the FBB(-) group across the entire cortex; especially in the frontal cortex, temporal cortex, anterior and posterior cingulate gyri and subcortical regions; precuneus and putamen (Table3.2).

However, there were no significant differences observed between the FBB(-) and FBB(+) group in the caudate nucleus and thalamus (Table 3.2).

TABLE 3.2: Quantitative PET data analysis by brain region

	FBB(+)group Est.mean SUVR (95% CI)	FBB(-)group Est.mean SUVR (95 % CI)	Mean Difference (95% CI)	T,p
Neocortex	1.44[1.37 - 1.5]	1.08[1.04 - 1.11]	0.36[0.28 - 0.44)]	9.67, p<0.00001
Frontal Cortex	1.37[1.25 - 148]	0.99[-0.94 1.06]	0.37[0.24 - 0.50]	5.76, p<0.00001
Temporal Cortex	1.62[1.52 - 1.72]	1.14[1.09 - 1.19]	0.48[0.37 - 0.59]	8.739, p<0.00001
Occipital Cortex	1.21[1.11 - 1.33]	1.1[1.05 1.17]	0.11[-0.015 - 0.24]	1.764, 0.0841
Anterior Cingulate	1.59[1.51 - 1.67]	1.19[1.15 - 1.23]	0.40[0.31 - 0.49]	8.882, p<0.00001
Posterior Cingulate	1.68[1.57 - 1.79]	1.19[1.14 - 1.26]	0.48[0.36 - 0.61]	7.90, p<0.00001
Precuneus	1.68[1.58 - 1.79]	1.13[1.08 - 1.19]	0.55[0.43 0.67]	9.27, p<0.00001
Caudate Nucleus	0.82[0.75 - 0.89]	0.78[0.75 - 0.83]	0.032[-0.05 - (0.12)]	0.79 , 0.44
Putamen	1.68[1.59 - 1.77]	1.39[1.34 1.44]	0.29[0.19 - 0.40]	5.63, p<0.00001
Thalamus	1.15[1.05 - 1.25]	1.07[1.02 - 1.13]	0.076 [-0.03 -(0.18)]	1.39, 0.17

The estimated means for each group [95% CI] are reported in Table 3.2, along with the estimate of the differences in the means between the two groups which were derived using the lm function in R studio (version 3.0.2) $(https://www.rstudio.com/)$. R studio is a statistical computing and graphic software employed in this study to perform statistical analysis. The T and P values of the differences between the group means are reported. Results from the ROI analyses are presented as Boxplots in Figure 3.2.

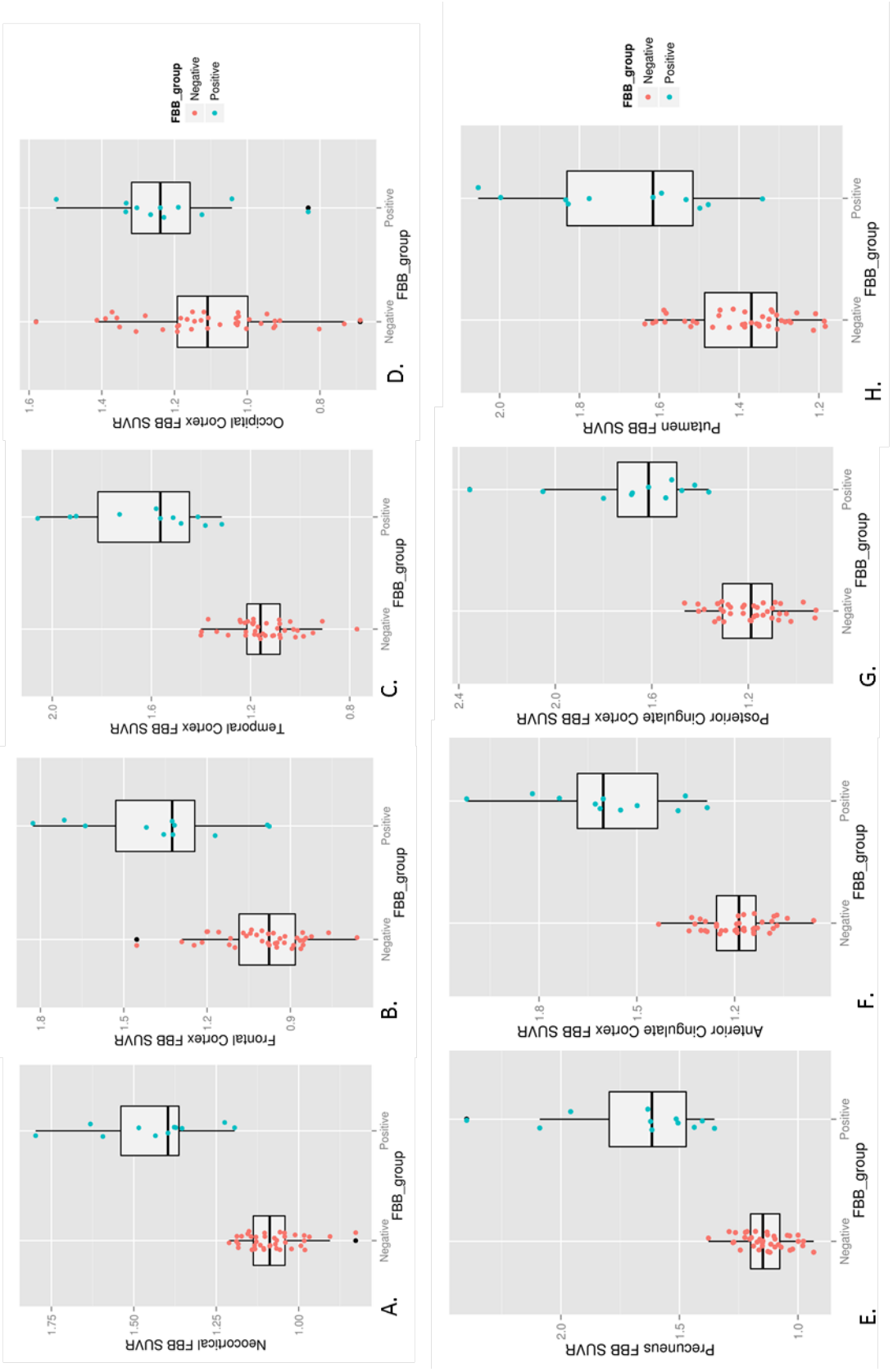

FIGURE 3.2: Regional Cortical uptake of FBB among the two Clinical classified groups (Amyloid-positive or Amyloid-negative). (A) Composite Cortical (B) Frontal cortex (C) Temporal Cortex (D) Occipital Cortex (E) Precuneus (F) Anterior Cingulate Cortex (G) Posterior Cingulate cortex (H) Putamen SUVR difference between the two clinical Classification. (Note: that the y-axis varies for different region)

3.2.1 Association of Global Amyloid Burden with Clinical and Neuropsychological scores.

We further investigated the relation between the SUVRs (regional and global) and the cognition parameters of the neuropsychological tests (i.e. global cognition Z score (a measure of global cognitive ability derived from the entire neuropsychology battery), MoCa score (cognitive assessment), individual cognition domain score (attention, executive, learning, language and visuospatial) and the Parkinson's disease dementia "risk" score (PDDRS) (Table 2.1). PDDRS is a Gaussian Process model used to acquire the probability of conversion to dementia within the next four years. This model was trained on an independent group of PD patients followed over four years and is based on age, MoCa and the test from the neuropsychology battery. Based on this model, the PDDRS was calculated in every PD-MCI patient. We chose the global cognitive Z score because it provides the best summary measure of the 4-6 hours of neuropsychology battery. To further understand the association between our data and cognition, we chose to look at each individual cognitive domain scores separately.

In the case of cortical and subcortical regional SUVRs, there was no evidence of correlation between sex (p-value = 0.56 and CI95: [-0.09 - (0.17)]), age (p-value = 0.17 and CI95: [-0.003 - (0.01)]), MoCa (p-value = 0.31 and CI95:[1.012 - (2.00)]), global cognition Z score (p-value = 0.94 , CI95:[-0.86 - (0.081)]) and PDDRS (p-value = 0.85 , CI95:[-0.13 - (0.64)]).

However, there was a group-by-Cog Z interaction, for the Amyloid-positive group, some of the regions SUVRs were slightly, but significantly, correlated with Global cognition Z score (CogZ) (Table 3.3). These regions were: Neocortical (Figure 3.3A), anterior cingulate, posterior cingulate and precuneus (Figure3.4A). These same regions, except for the precuneus, also showed a significant interaction with PDDRS (Table 3.3). For all these region, the correlation between SUVR and global cognition Z score was negative; meaning that the higher the retention of FBB in a given region, the lower the cognition Z score was in the FBB(+) group. No significant correlation between SUVRs and global cognition Z score were found in the FBB(-) group (Figure(3.3a)). The correlation between the SUVRs for the aforementioned regions and PDDRS were positive,

which shows that with an increase of FBB retention in a given region, the probability of a future dementia increases (Figure (3.3c)). Another observation made for only the clinical amyloid-positive individuals, was that there was a significant correlation between SUVRs in the composite cortical, posterior cingulate and anterior cingulate regions and MoCa test score. For all three regions the association in the FBB(+) group was highly significant: cortical region (p = 0.004, CI95:[-0.05 -(-0.011)](figure3.3B), posterior cingulate (p = 0.02, CI95:[-0.083 -(-0.0075)]) and anterior cingulate(p = 0.01, CI95:[-0.065 -(-0.009)]). Similar to the global cognition Z score correlation for FBB(+) group, the correlation between these regions and MoCa was negative. No significant correlation was found in the FBB(-) group.

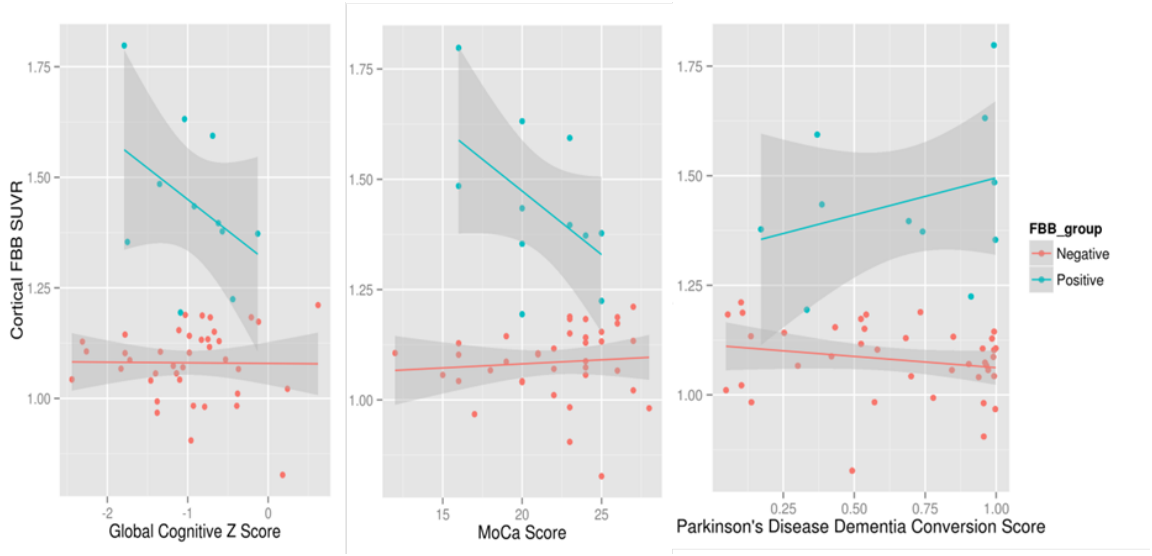

FIGURE 3.3: Plots of interaction between FBB group and (A.) Global Cognitive Z score (B.) MoCA Score (C.) Parkinson's Disease Dementia Conversion Score. Across all 3 measures, there was a significant interaction. The FBB(-) group showed no association with cortical SUVR, while the FBB(+) group showed a significant association with CogZ, MoCa and PDDRS.

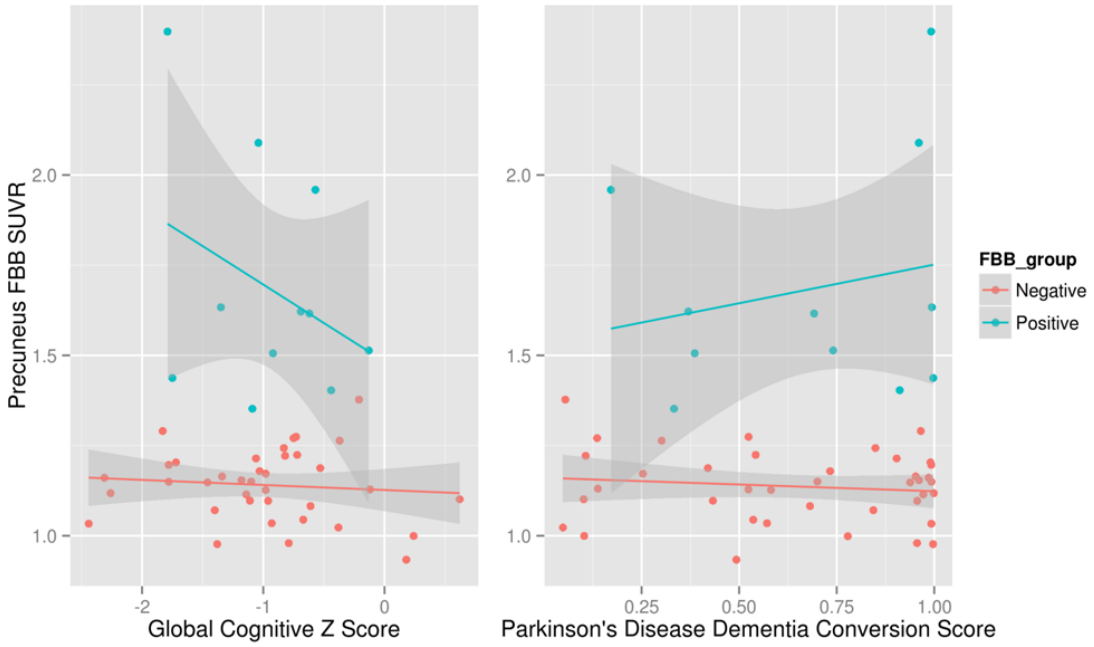

FIGURE 3.4: Association between the Precuneus FBB uptake (SUVRs) with (a) the Global cognition Z score and (b) Parkinson's Disease Dementia "conversion" score.

There were however, no significant association or interaction found between regional SUVRs in the caudate nucleus (Figure 3.6), putamen Figure(3.5), or thalamus, and PDDRS and Global cognitive Z score (Table 3.3).

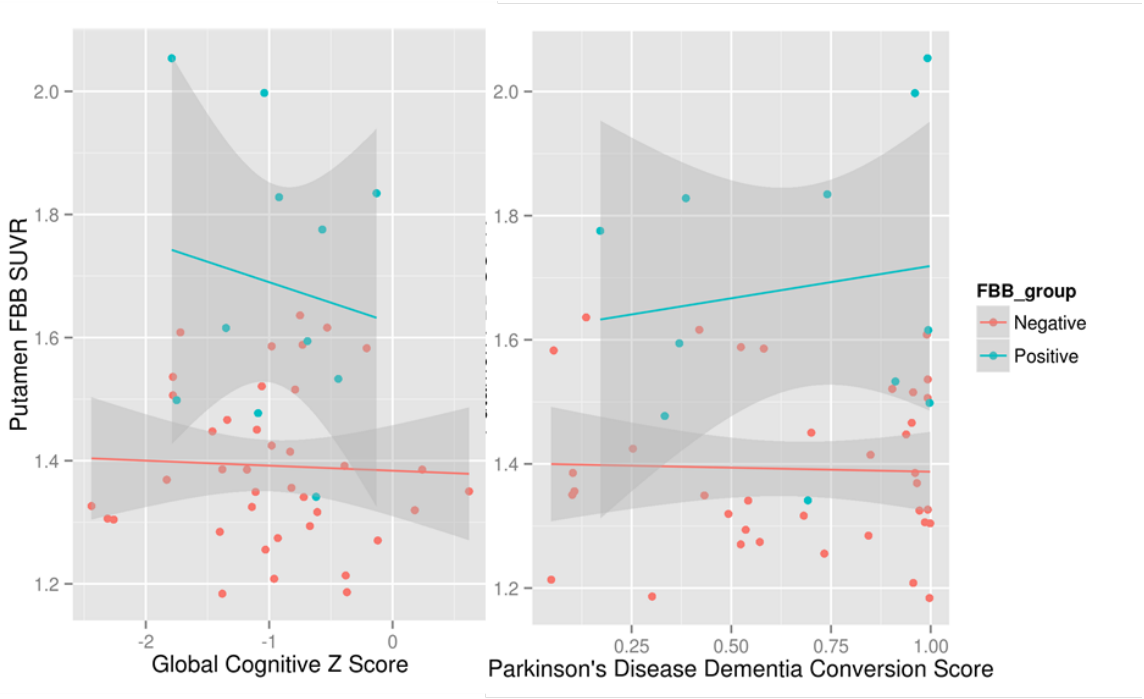

FIGURE 3.5: Non-significant association between the Putamen FBB uptake (SUVRs) with CogZ and Parkinson's disease dementia "conversion" score.

TABLE 3.3: Regional SUVR group-by-cog score interaction correlation for Clinically classified Amyloid-positive participants with Parkinson's Disease Dementia conversion score and Global cognitive Z Score

	PDDRS Correlation T(p-value)	Global Cognitive Z Score T(p-value)
Neocortex	1.70(0.09)	-2.42(0.020)
Anterior Cingulate	1.71(0.009)	-1.71(0.084)
Posterior Cingulate	1.14(0.26)	-1.95(0.057)
Precuneus	1.24(0.10)	-2.09(0.043)
Caudate Nucleus	0.26(0.79)	-0.24 (0.8)
Putamen	0.66(0.08)	-1.23(0.22)
Thalamus	-0.07(0.94)	-0.48(0.63)

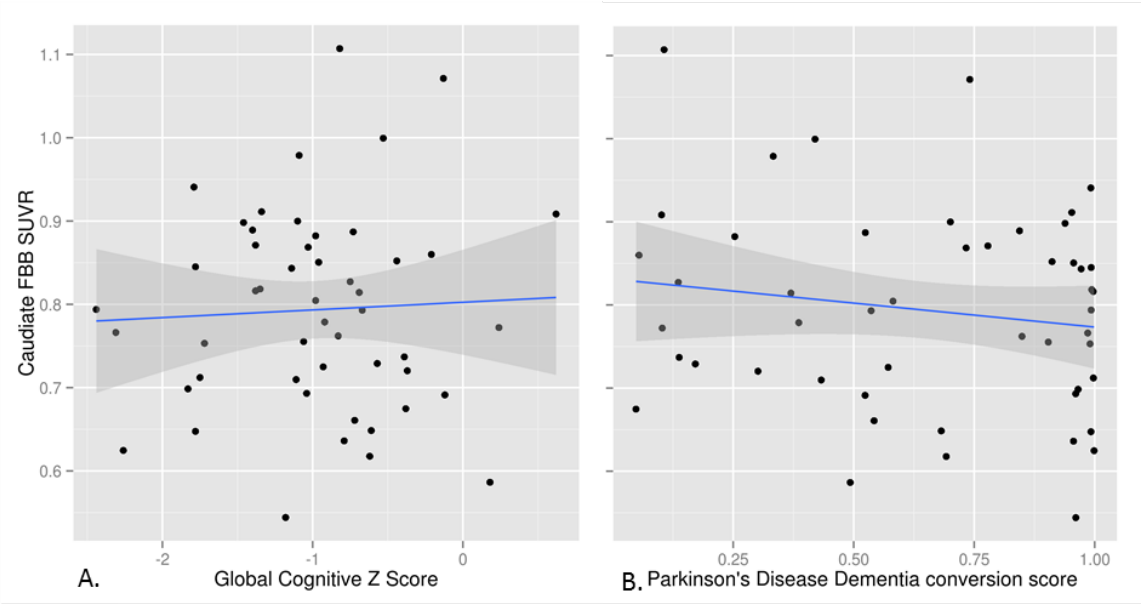

FIGURE 3.6: Association (not significant) between the Caudate Nucleus FBB uptake (SUVRs) and (A) Global Cognitive Z Score and (B) Parkinson's disease dementia "conversion" score.

3.3 Principal Component Analysis

PCA was applied to identify the pattern of regional FBB uptake (amyloid accumulation) in PD-MCI. From the PC analysis, the first five components were investigation, which cumulatively explained 68.9% of the variance in the data. Principal components 1, 2, 3 ,4 and 5 explained 30.3%, 16.9%, 11.8%, 6.2%, 3.8% of the variance, respectively. Axial, sagittal and coronal slices of all five PCs are illustrated in Figure 3.7. The first principal component showed a significant difference between the FBB(+) group and FBB(-) group and was characterized by increased FBB retention in the cortex (Figure 3.7a). The second component showed the difference between the FBB(+) and FBB(-) group through increased FBB retention in the preforntal cortex, anterior cingulate, posterior cingulate and the temporal cortex (Figure3.7B). The third component was driven from the variation within the white matter and FBB retention in the brainstem, thalamus, putamen and caudate nucleus (Figure 3.7C). The fourth component highlighted the relative difference between the frontal cortex and the rest of the brain (Figure 3.7D). Finally, the fifth component demonstrated specifically the FBB retention in the thalamus (Figure 3.7E).

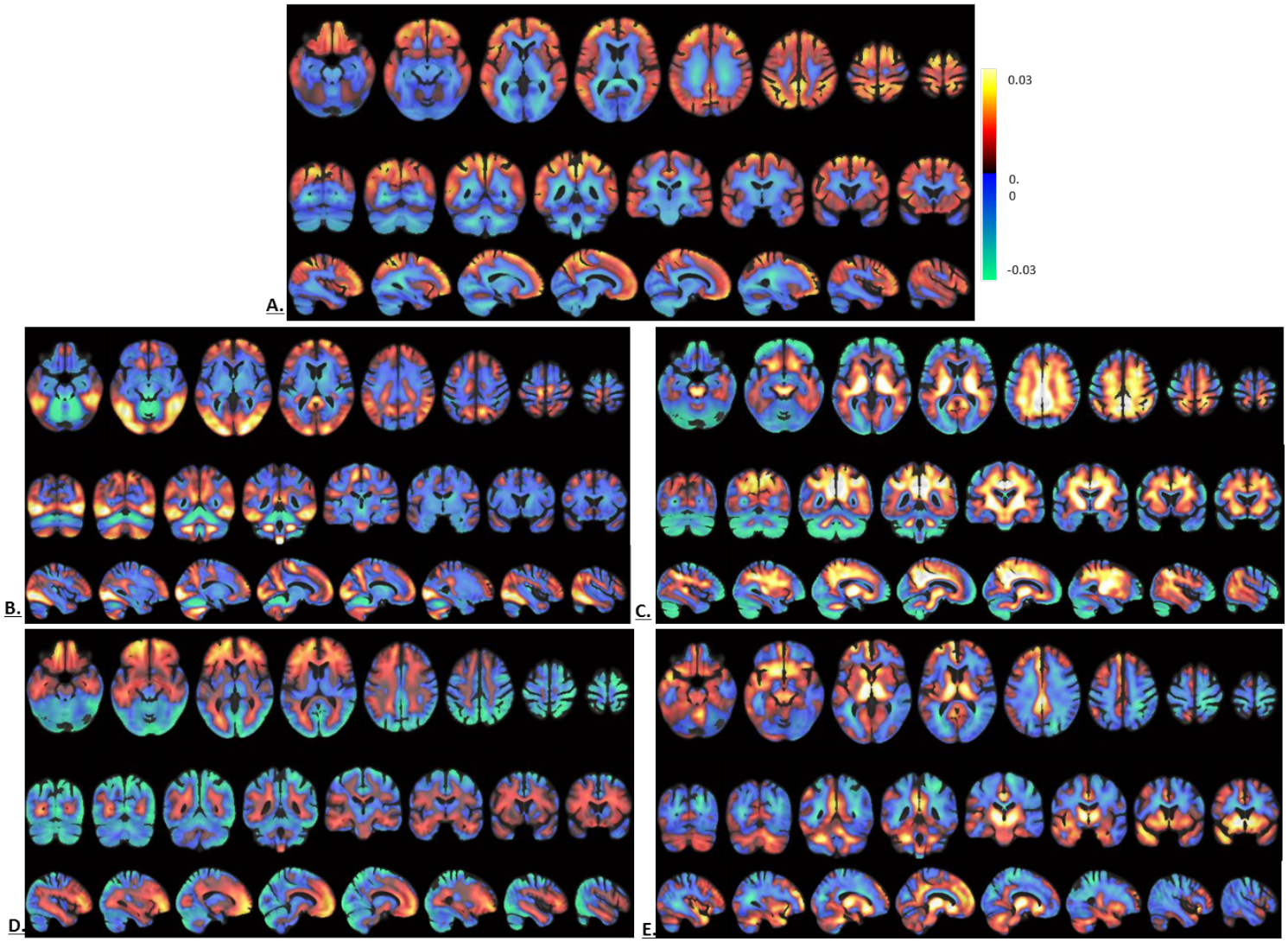

FIGURE 3.7: First five Principal Component images of our dataset representing majority of the variance in our dataset. (A) Principal Component 1 (variance = 30.2%, eigenvalue = 4.11) , (B) Principal Component 2 (variance = 16.8%, eigenvalue = 2.28) , (C) Principal Component 3(variance = 11.8%, eigenvalue = 1.60), (D) Principal component 4 (variance = 6.2%, eigenvalue = 0.84) and (E) Principal Component 5 (variance = 3.8%, eigenvalue = 0.51).the colour bar indicates the relative intensity at each voxel for the principal components.

3.3.1 Principal Component association with Clinical classification and Neuropsychological score

The association of the five principal components was with the clinical classification, illustrated in Figure 3.8.

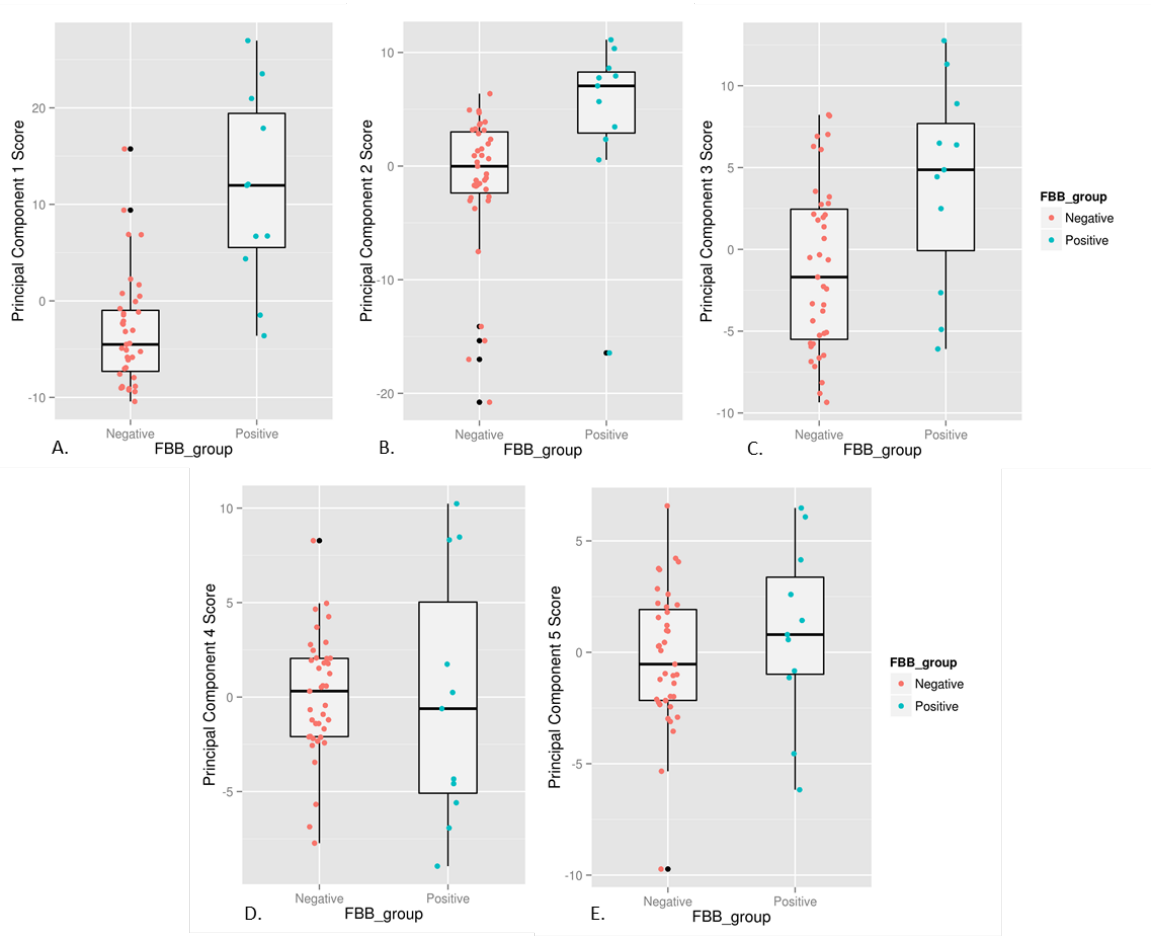

FIGURE 3.8: Association between the Principal Component and the clinical classification

A stepwise logistic regression identified three components (PC 1, 2, 3) to be significantly associated with the clinical FBB groups (Table 3.4).

We applied multiple regression using age, sex, disease duration, UPDRS-III, CogZ/PDDRS to the first five principal components. In the case of principal component 1 (PC1): there was no correlation with the global cognitive z score or the PDDRS.

However, there was a significant association with age (t = 3.605, p = 0.0007, CI95:[3.1 -(11.1)]), sex (t = 2.023,p = 0.05, CI95:[0.04 -(12.6)]) and UPDRS (t = 2.64, p = 0.011,

TABLE 3.4: Association between the FBB group and the PC scores

	Mean difference between FBB_groups(SD)	T,p	95% confidence interval [CI95]
Principal Component 1	14.70(2.30)	6.28(9.34e-8)	[9.99-19.40]
Principal Component 2	5.65(2.21)	2.55(0.014)	[1.20-10.09]
Principal Component 3	5.13(1.82)	2.81(0.007)	[1.45-8.80]
Principal Component 4	-0.23(1.43)	-0.16(0.87)	[-3.10-2.64]
Principal Component 5	1.09(1.11)	0.99(0.33)	[-1.13-3.33]

CI95:[0.05 -(0.42)]). Furthermore, when looking at the amyloid-positive group PC1 score, found a significant negative correlation with both the learning domain (t = -2.59, p = 0.013, CI95:[-12.68- (-1.57)]) (Figure 3.9A) and the MoCa score (t = -2.18, p = 0.035, CI95:[-2.87 - (-0.11)]) (Figure 3.9B).

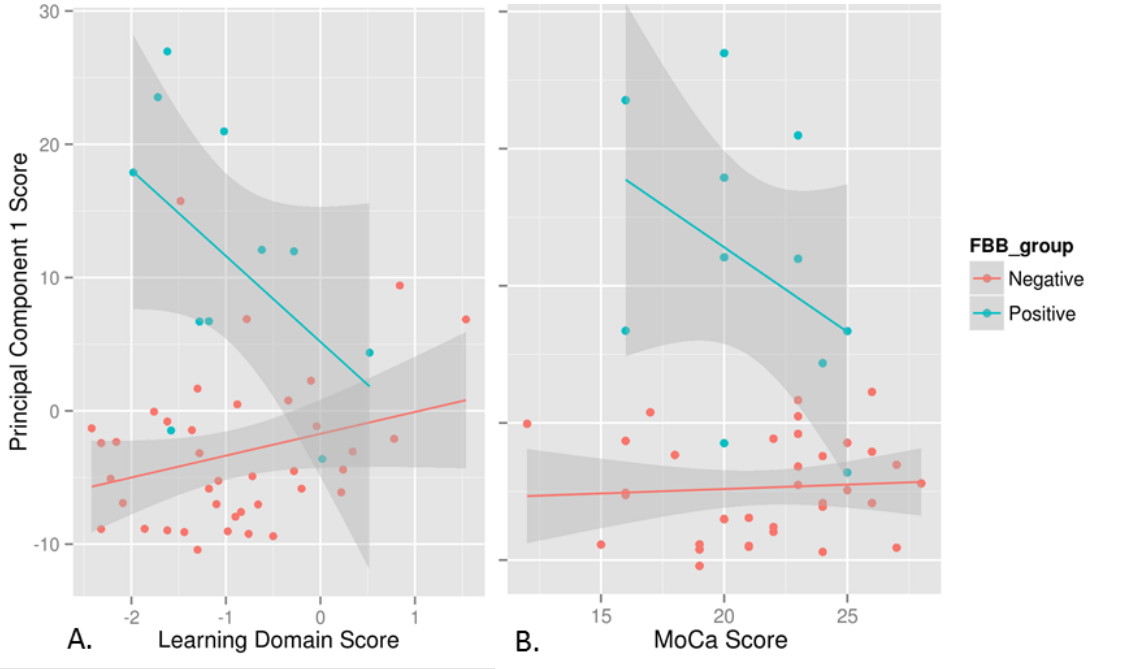

FIGURE 3.9: Principal Component 1 score correlation with (A) Leaning Domain score (r = 0.58, t = -2.59, p = 0.013, CI95:[-12.68-(-1.57)]) and (B)MoCa Score (r = 56, t = -2.18, p = 0.035, CI95:[-2.87 - (-0.11)]).

In the case of principal component 2 (PC2), there was no correlation with age, sex , UPDRS, the global cognitive Z score or PDDRS. However, the amyloid positive group PC2 score showed a significant negative correlation with the executive domain (r = 0.45, t = -2.86, p = 0.007, CI95:[-16.06 -(-2.77)]) (Figure 3.10).

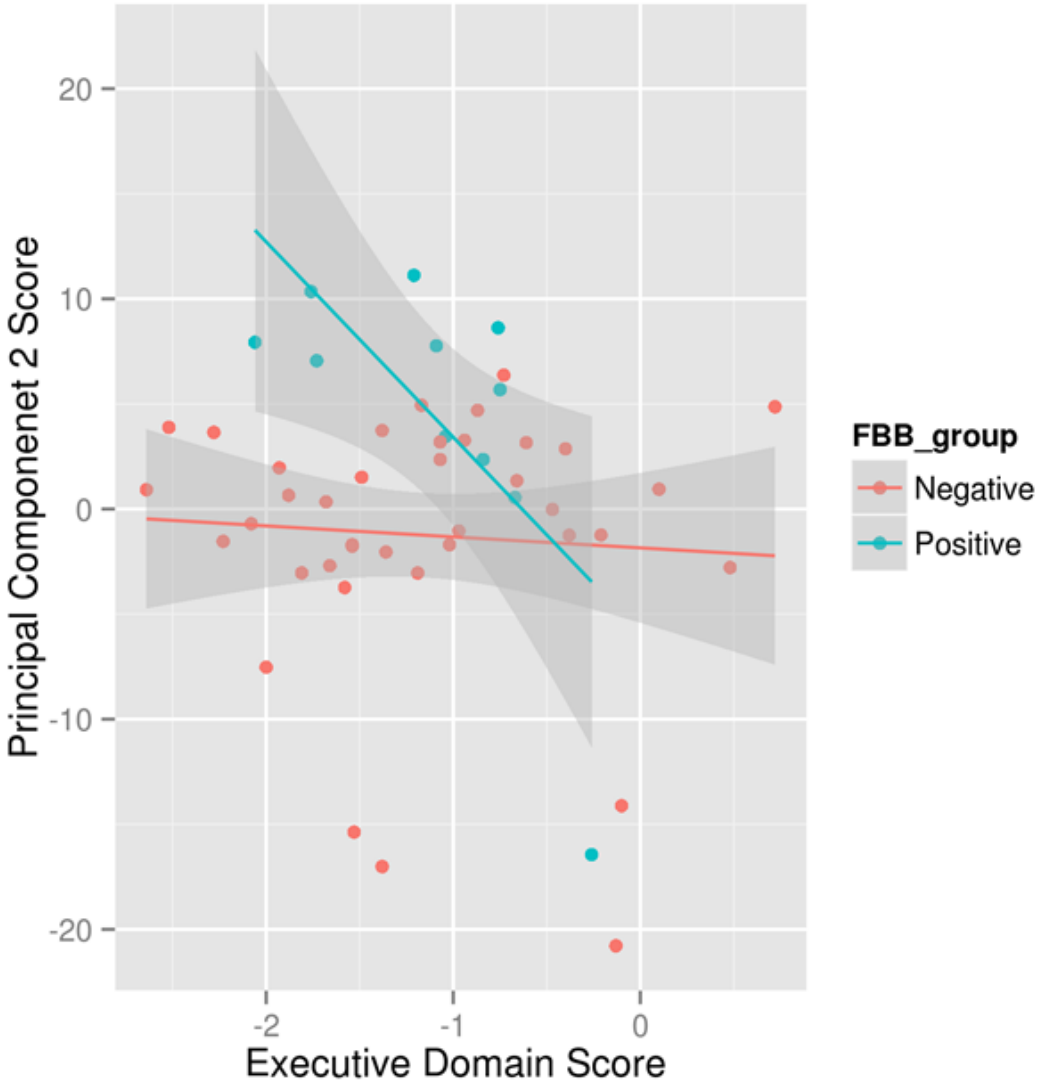

FIGURE 3.10: Principal Component 2 score correlation with Executive Domain score (r = 0.45, t = -2.86, p = 0.007, CI95:[-16.06-(-2.77)])

In the case of principal component 3, there was a slight, but significant correlation with sex (t = 1.98, p = 0.05, CI95:[-0.05-(7.84)]). For principal components 4 and 5, no correlations were observed with any of the cognitive parameters. However, an interesting correlation was observed in the case of principal component 4 (PC4). PC4 showed significant negative correlation with white matter hyperintensity lesion volume (r = 0.16, t = -2.73, p = 0.009, CI95:[-2.94 -(-0.44)]) (Figure 3.11).

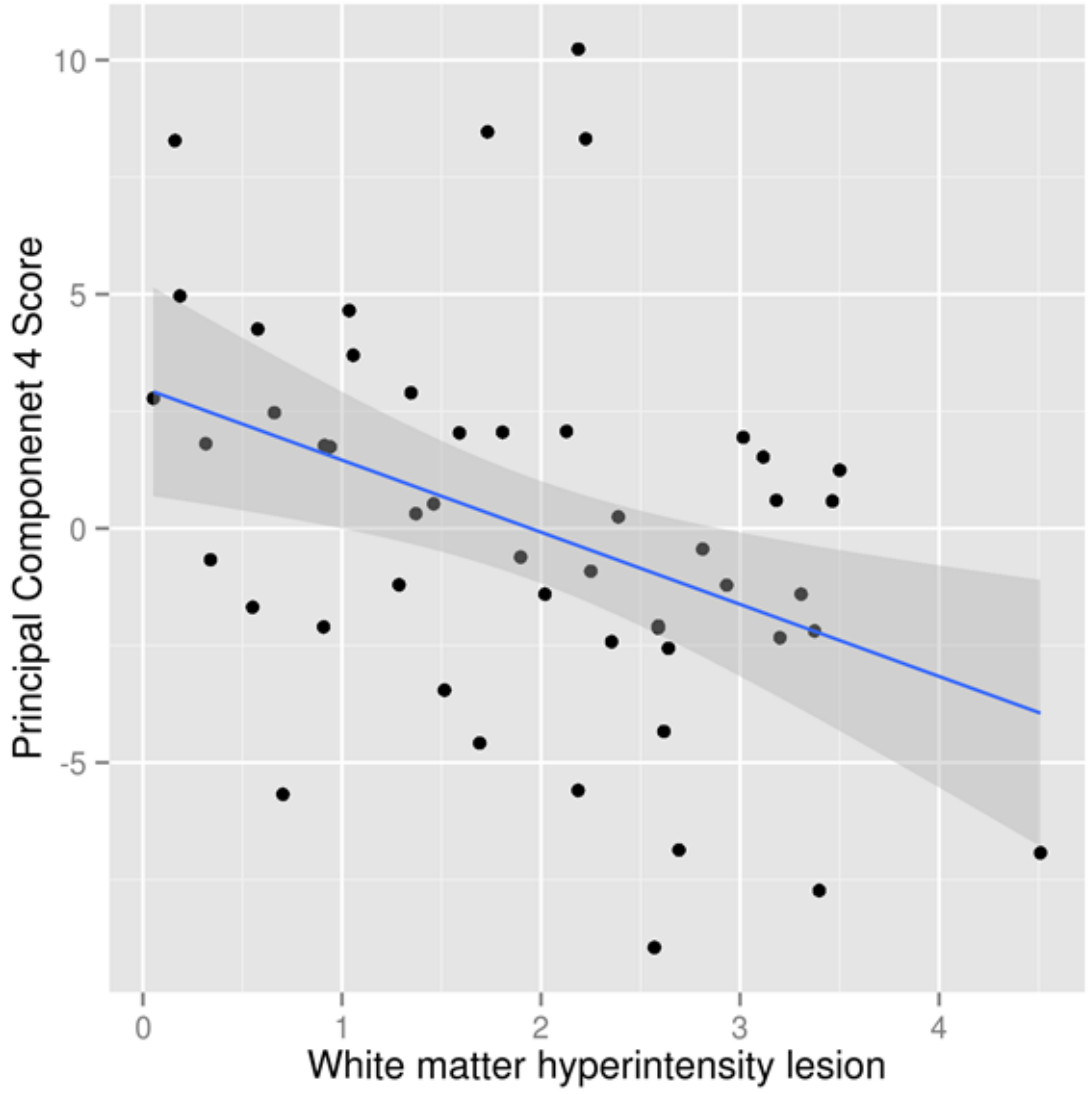

FIGURE 3.11: Principal Component 4 score correlation with White matter hyperintensity lesion (r = 0.16, t = -2.73, p = 0.009, CI95:[-2.94 -(-0.44)])

3.3.2 Clinically Classified Amyloid-related Network

Since the first three components were significantly associated with the clinical classification, a linear combination of these components was used to form a network. This network, gives a better representation of amyloid deposition than a single PC in this sample. To acquire this network score, linear regression was employed (equation3.1). The β parameters (β = 0.0307, -0.0212, 0.0275) were taken from the results of the stepwise logistic regression (FBB group was taken as the dependent variable and the PC1,

2, 3, 4 and 5 scores were the independent variables).

$$network(score) = \beta + \beta 1PC1 + \beta 2PC2 + \beta 3PC3 \tag{3.1}$$

The network image is illustrated in Figure 3.9. It is characterized by increase FBB retention in the cortical regions relative to the deep white matter. It showed high retention in the temporal cortex region, frontal cortex region, putamen, precuneus, anterior and posterior cingulate regions.

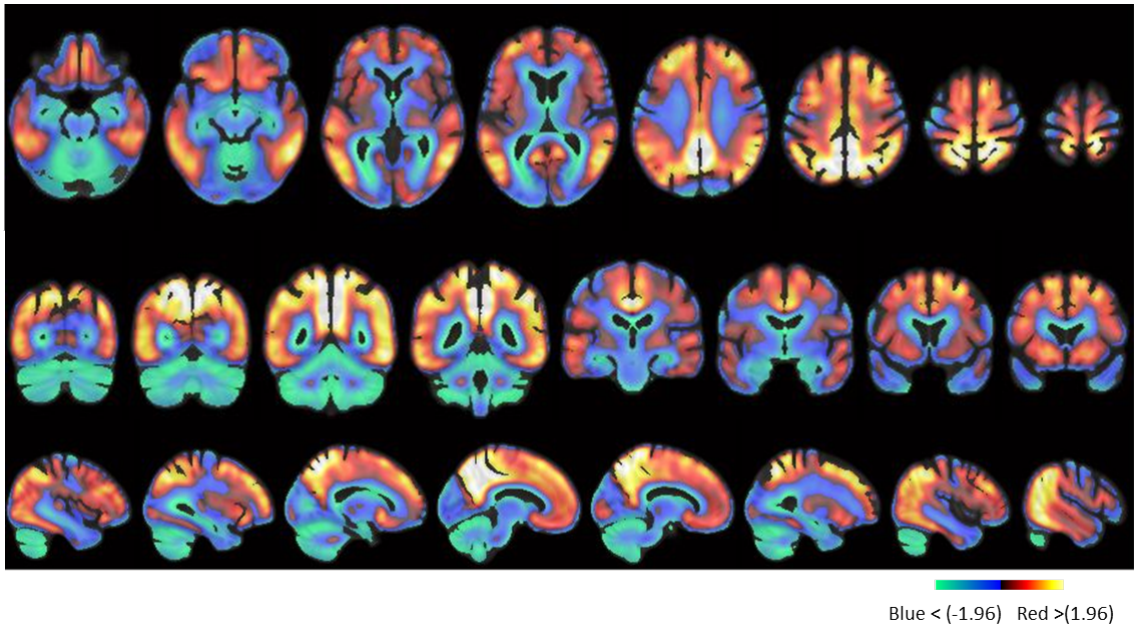

FIGURE 3.12: Clinical classified Amyloid-positive or negative group related PC Network Image. colour bar indicates the level of amyloid accumulation, the Yellow/red regions are high amyloid accumulation (FBB retention) and the blue regions are no FBB retention

3.3.3 Network Image correlation with the cognitive parameters

The association of the PC network score with the CogZ was investigated, which showed a highly significant group-by-cognition interaction, where the amyloid-positive group showed a negative correlation with the global cognitive Z score (r= 0.75, t = -2.21, p = 0.033, CI95:[-0.52 -(-0.023)]) (figure 3.13A) and also with MoCa score (r= 0.75, t = -2.56,

p = 0.014, CI95:[-0.09 -(-0.011)]) (figure 3.13B), No such correlation for the FBB(-) group was found.

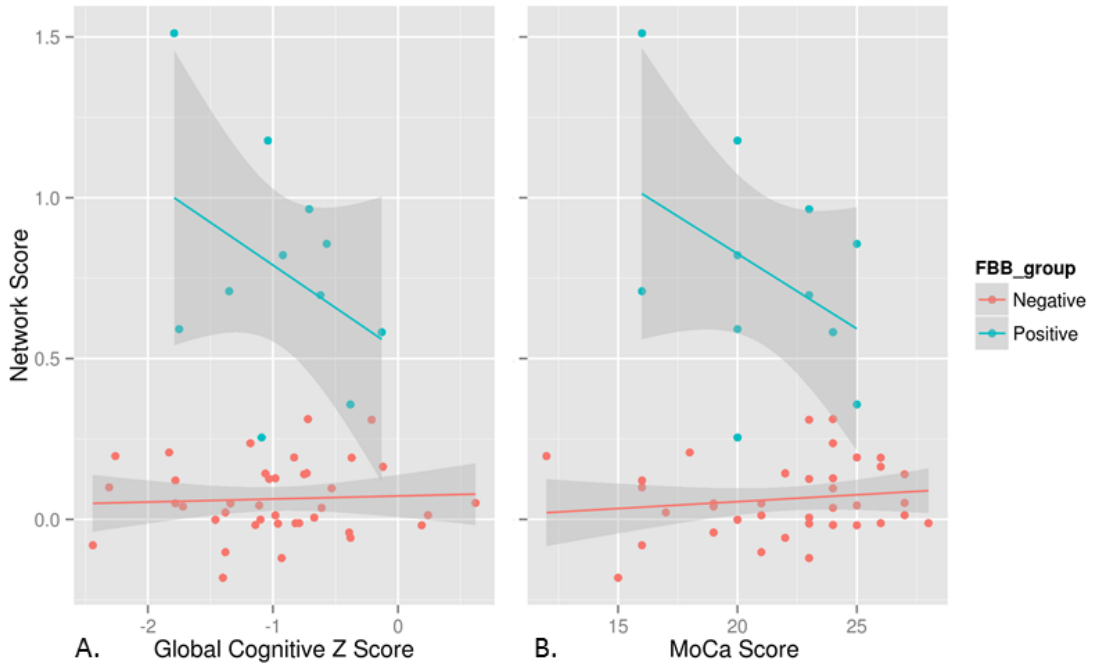

FIGURE 3.13: Network score group-by-cognition interaction with Global cognitive Z Score (t = -2.21, p = 0.033) and MoCa Score (t = -2.56, p = 0.014)

3.4 Independent Component Analysis

In ICA, the components are not orthogonal and are not ranked according to the relevance of the component. So, in order to understand the pattern of variance and the pattern in our data set, we need to look at all the components separately. In this study, 25 components were acquired , from which 17 components showed an association with the clinical classification of the individuals. However, none of the components were able to provide any association with the cognitive parameters. Since, it was unable to provide any association with the neuropsycological test scores, I didn't look further into the ICA.

3.5 Bootstrapping

In order to test the reliability of our PC-Network, SUVR PET images were randomly sampled with replacement, to form a resampled data set of the population of 50 PET images. Bootstrapping was applied 5000 times and each time a new network image was generated with the new resampled data. The 5000 network images were averaged and an approximate standard deviation of the resampled population was obtained. Using the approximate standards deviation and the mean image we acquired Z-scores for each voxel. A threshold value of 1.96 was set to obtain regions which significantly contribute to PD pathology.

The Z-score image (Figure 3.14) provided much more clarity and provides robustness in the association between these regions shown in red in Figure 3.14 with amyloid deposition in PD-MCI. It showed that most of the amyloid accumulation was observed in the temporal cortical region, precuneus region and the anterior cingulate. There was no significant uptake in the putamen or caudate nucleus.

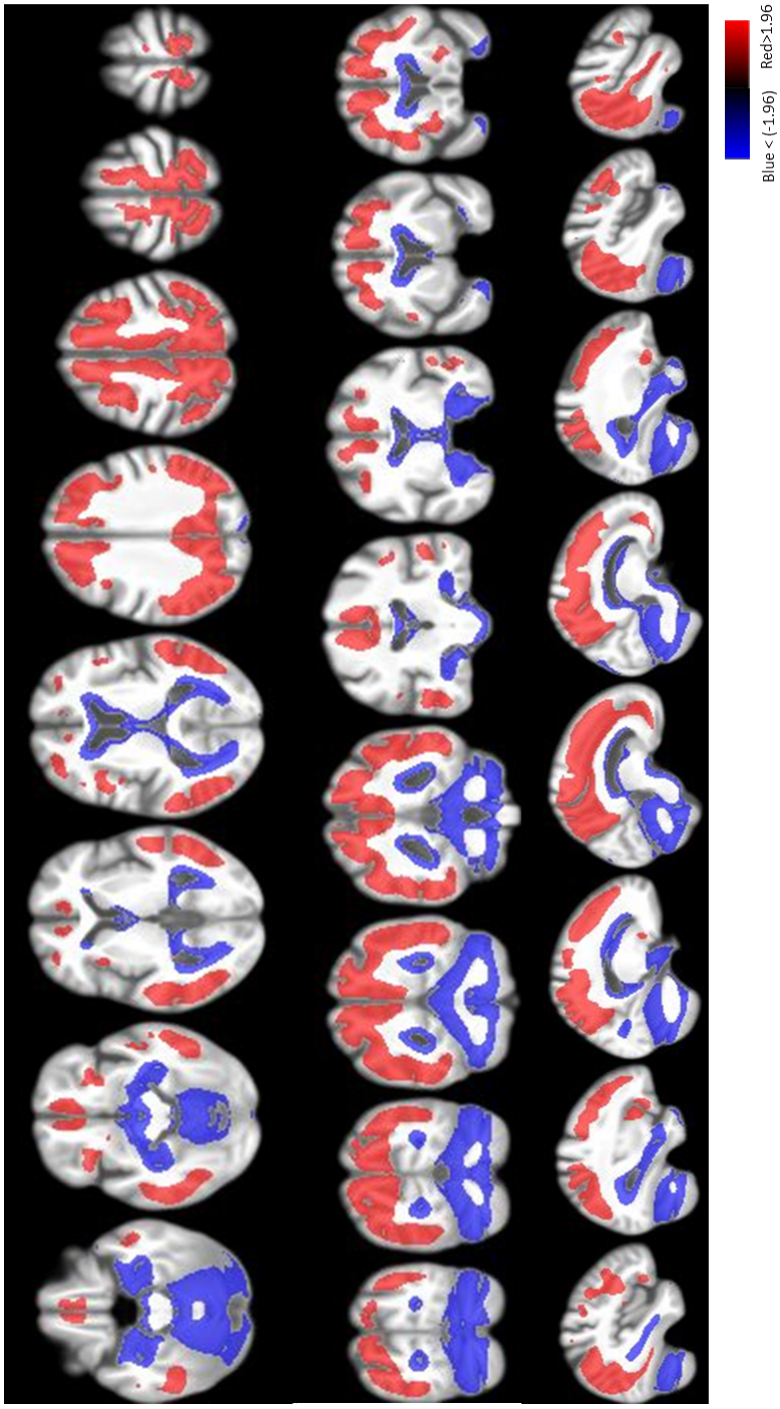

FIGURE 3.14: Z-score image representing the regions(RED) of amyloid accumulation in PD-MCI,shown to be robust through bootstrap sampling (Z > 1.96, p< 0.05). And region (blue) shown low amyloid accumulation relative to the Red region (Z < -1.96 , p-value < 0.05)

Chapter 4

Discussion

Patients with PD have an increased risk of advancing to dementia. Cognitive impairment is now seen as a major feature of PD. It is most likely a result of a complex interplay of pathology including alpha synuclein pathology, AD pathology (tau, β amyloid) and neurotransmitter dysfunction (Silbert & Kaye, 2010). These pathologies may accelerate each other to worsen the state of the disease. In recent years, the role of β amyloid has been a focus for research on cognitive impairment in PD.

Our study, showed that FBB-PET imaging allows $invivo$ visualization of amyloid deposition in PD. Specifically, 11 subjects (22%) from the PD-MCI group at baseline showed AD-type neocortical FBB-binding, which may contribute to an increased risk of developing dementia. Our finding was slightly different than an earlier finding by Pedersen. et.al.; According to their study, 27% of PD-MCI cases exhibited amyloid positive scans (Pedersen, Larsen, Tysnes, & Alves, 2013). However, a different group showed only 15% of their population of 40 PD-MCI exhibited AD-type neocortical PiB binding (Petroou, Bohnen, Muller, Albin, & Frey, 2012). On the other hand, our study was in agreement with the previous studies, on the basis of the regions associated with AD-type amyloid deposition in PD. These regions were neocortical, frontal and temporal cortex, anterior and posterior cingulate, precuneus, caudate nucleus and thalamus as seen in figure 3.14.

From our quantitative PET data analysis in section 3.2, we were able to show increased uptake of FBB in a group clinically classified as amyloid-positive, relative to those classified as amyloid-negative (Table 3.2). A significant difference in the uptake of FBB

between the two classes was observed in multiple regions: composite neocortical region, frontal cortical region, temporal cortical region, posterior cingulate, anterior cingulate, putamen and precuneus. However, we found no significant difference in the uptake of FBB between the two groups in the caudate nucleus and thalamus. The finding of increased FBB in the putamen, but not the caudate is interesting. Goldstein et.al. showed lower F-DOPA uptake in the putamen compared to the caudate nucleus (Goldstein, Holmes, Sewell, & Kopin, 2009), indicating large deficit in the putamen. The dopamine pathway appears to deteriorate earlier in the putamen in comparison to the caudate nucleus. The increased FBB and decreased dopamine indicates that the putamen is particularly hard hit in PD; showing the contribution of AD-pathology and neurotransmitter deterioration "working together" in the progression of the disease.

Region of interest analysis and global analysis confirmed that there was a significant group-by-cognition interaction, showing that the neocortical uptake of FBB was significantly correlated with the global cognitive Z score only in the FBB(+) group (figure 3.3). However, this relation did not exist in the amyloid-negative group. This suggests that amyloid accumulation may contribute to cognitive impairment but only after a threshold is reached. Or it could be that variation in low β-amyloid levels, i.e. sub-threshold, have no effect on cognitive ability. However, as the presence of amyloid plaques begin to accumulate, this could start to contribute to cognitive deterioration along with other pathological processes. We observed a negative correlation between amyloid accumulation and cognitive impairment, meaning with higher amyloid accumulation in the neocortial region, worse global cognitive impairment was observed. This association was also observed in previous studies, showing a higher PiB retention associated with worse global cognitive impairment (Petroou et al., 2012) and (Gomperts et al., 2013). Similar correlations between FBB uptake and global cognitive Z score were made in the: anterior cingulate, posterior cingulate and precuneus. This shows the importance of these region for cognition and the association of amyloid accumulation with cognitive decline in PD-MCI.

We also showed significant association between amyloid accumulation and Parkinson's disease dementia conversion score (probability of PD conversion to dementia

within four years). This is a positive step towards showing the contribution of amyloid accumulation to the development of future dementia in PD-MCI, indicating that amyloid deposition may be a contributing factor to the development of future dementia in PD.

We used multivariate data analysis method (principal component analysis) to identify the pattern of amyloid accumulation in PD that best separates the FBB(+) and FBB(-) group. Prior to our study, only a few studies have used PCA to understand the distribution of PiB in PD and AD (Campbell et al., 2013).

We analysed components that in total captured 66% of the variance within our data. For this study, the principal components 1, 2, 3 ,4 and 5 collectively explained 68.9 % of the variance in the data set. Each of the principal components encompassed a different pattern of amyloid accumulation. Principal components 1, 2 and 3 all showed an association with the clinical classification of amyloid positivity. In order to understand the PD-related pattern of amyloid accumulation, I employed linear combination of principle components 1, 2, and 3 to derive a pattern of amyloid distribution that best separated FBB(+) and FBB(-).

Principal component 1 showed an association with learning ability and acquiring new information indicating that the pattern of FBB accumulation affected learning and memory. The pattern of uptake for principal component 1 was similar to the pattern of uptake seen by Campbell et al. i.e. FBB retention in the cortical region (Campbell et al., 2013). Furthermore, we also showed a positive correlation between principal component 2 FBB uptake pattern and executive domain impairment for FBB(+) group. Higher accumulation of amyloid in the temporal cortex, prefrontal cortex and anterior and posterior cingulate was associated with the worsening of an individuals ability to solve problems and plan for the future. This finding is consistent with the anatomy of executive function, as the area of the brain that plays an important role in executive function is the preforntal cortex (Katz, Zafonte, & Zasle, 2006). So an abnormality in this region (e.g. excessive amyloid deposition) may result in executive dysfunction.

Principal component 3 and 5, driven from variation in white matter and FBB retention

in the thalamus, respectively, showed no relation with the neuropsychological cognition test and other tests measured in our group. This is an interesting finding in that the thalamus is an important structure for effective cognitive processing. ROI analysis showed that the thalamus was relatively spared by amyloid deposition, suggesting that structural (Melzer et al., 2012) and diffusion (Melzer et al., 2013) deficits underlying cognitive dysfunction are not influenced by amyloid pathology in the thalamus. However, component 4 showed a very interesting relationship with the white matter hyperintensity lesion volumes. A study conducted by Chao et.al, showed a similar association in which individuals with WMH pathology were more vulnerable to the effect of AD pathology and amyloid-β deposition in cortical regions (Chao et al., 2013). β-amyloid is known to cause oxidative damage and results in the formation of free radials and damage to oligodendrocites. Furthermore, an initial elevation of amyloid-β results in damage to the white matter which in turn causes increased level of β-amyloid (Gordon, d Phillip Hsu, Roe, Morris, & Benzingera, 2015). Therefore, the extent of white matter lesions could predict the level of amyloid accumulation and perhaps provide an indirect measure of β-amyloid deposition.

As mentioned earlier, a network indicating the distribution of increased amyloid accumulation was created. It showed the specific pattern of regional uptake in the brain associated with amyloid accumulation. Prominent regions with amyloid accumulations included the temporal cortical region, medial frontal cortical region, precuneus, putamen, anterior cingulate and posterior cingulate. This finding is consistent with the previous studies and also resembles an "AD like accumulation pattern". However, the network showed that the hippocampus in our data was not included in the areas associated with high level of β-Amyloid (the blue region in figure 3.14). This shows that amyloid accumulation in PD may not necessarily be the same as that expected in AD. However, this was not directly compared, therefore, future studies directly comparing amyloid accumulation in PD-MCI and AD-MCI would help to confirm our initial observation.

The network score for the amyloid-positive group showed an association with the global cognitive Z score and also the MoCa score (figure 3.13). However, it showed

no association with the Parkinson's disease dementia conversion score (PDDRS). It is interesting to note that the network score was associated with the cognition Z score but not with the PDDRS. This indicates that the cortical amyloid deposition may impact current cognitive status, but may not provide information about future status. However, PDDRS is a prediction and we would have to wait and see if any of the current PD-MCI participant develop dementia over the course of the next 3 years. This is exactly what this continuing study intend to do. PD-MCI participants will now be followed to determine whether they do in fact develop dementia. Future work would then investigate whether baseline FBB scans contribute to the prediction of dementia development.

This study has some limitations which would be interesting to work on in the future. Since the sample were only PD-MCI , we did not obtain data from participants across the cognitive spectrum. Therefore, future research should look at comparing our results from PD-MCI to controls (PD-N and PDD). Also, since in this study we found the "AD like accumulation pattern" in some regions. It would be interesting to compare our PD-MCI findings with the AD-MCI population.

In this study we employed standard uptake value ratio (SUVRs) as our tool to calculate the radioactivity concentration for regions of interest. In future, it would be interesting to acquire arterial blood sampling for these participants, along with SUVRs. Arterial blood concentration is a measure which provides information of the concentration of the radiotracer as function of time (Phelps, 2004). This is important, as it is the concentration of radiotracer that feeds into various tissues (Phelps, 2004).

In the case of motion correction, we employed the second method (discussed in section 2.5.2), where we applied attenuation correction before motion correction. Even though, we obtained good quality images for our analysis, it would be interesting to work on the first method, where motion correction is employed before attenuation correction. Motion correction prior to attenuation correction, has been shown to provide better image quality in terms of visibility of possible amyloid deposition, size and contrast of images. I looked at the radon transformation method as a reconstruction tool for attenuated corrected sinogram, which reduced the image quality. However, I believe

by employing the iterative reconstruction method (which is employed by the image reconstruction in PET/CT scanner) we could potentially reconstruct images which will provide us with better image quality. We were unable to look at the iterative reconstruction method in this thesis as we did not have access to the specific software and were unable to manually apply this reconstruction method due to time constraints.

However, even though we has some limitations to this study. This study have one huge strength, which is the sample size of fifty PD-MCI participants. This sample size has previously never been examined to study amyloid burden in PD-MCI using amyloid-PET imaging.

Chapter 5

Summary

The aim of this thesis was to evaluate the use of FBB-PET imaging as a tool for $invivo$ visualisation of amyloid accumulation in PD-MCI. Another relative aim was to determine the association of amyloid accumulation with the cognitive decline and clinical evaluation in PD-MCI. The reason for this study was to contribute to the ongoing longitudinal study, in helping to predict which individuals with PD-MCI are at higher "risk" of developing dementia in the near future.

We showed that FBB-PET imaging may be an extremely valuable tool for assessing amyloid accumulation in PD. We found that around 22% of the PD-MCI in our study population showed amyloid positivity, suggesting that individuals with PD-MCI may have amyloid deposition. Using principal component analysis, I identified a pattern (regions) of amyloid accumulation in the PD-MCI patient, which were similar to that found in studies examining AD type amyloid deposition. These regions were: neocortical, frontal and temporal cortex, precuneus, anterior and posterior cingulate, caudate nucleus and thalamus. Impairment in executive function, attention, learning and memory appears to be associated with the accumulation of amyloid in the regions mentioned earlier.

Finally, this study was able to show that once amyloid plaque accumulation begins in the cortical and subcortical regions described above, it could start to contribute to cognitive deterioration in PD-MCI. Thus taking a positive step showing that amyloid deposition may play an important role in PD and the development of future dementia.

Appendix A

Matlab code for attenuation correction and Image reconstruction

```
% CT based ATTENUATION CORRECTION for PET
% 9/07/2015 - Guneet Kaur

% Before using this script to reconstrcut the attenuated corrected
% PET image.1) make sure that the TOFNAC PET images are realigned
% and a sum image is created .
% 2) downsample the CT image in order to co-register it to the PET
% and MR image .3) co-register the CT image and PET summed Image using
% SPM co-register batch.
% 4) make sure that both the CT and PET summed image is also
% co-registered to the MR structural (down sampled image 256X256)

%Load down sampled CT image to PET image
%Only works for 1 image at the moment.

[inputfile] = spm_select(1, 'image', 'Select down sampled CT image');
CT_im = spm_vol(inputfile);

% Load the PET image for teh same individual
input2 = spm_select(1, 'image', 'Select PET image');
```

```
PET_im  = spm_vol(input2);

%Read the CT and PET image.
CT = spm_read_vols(CT_im);
PET = spm_read_vols(PET_im);

%% This step is using the CT image only
% convert the HU value to linear attenuation coefficient (LAC) at 511 keV
% use the standard linear coefficient value for water and bone.

LAC = zeros(size(CT));

if CT<= 0

    LAC = (0.096.*(CT+1000))./1000;
else
    LAC = (0.096 + (CT.* ((0.184 .*(0.172 -0.096))./(1000.*(0.428 - 0.184)))));

end

LAC;

%%
% Eliminate the linear attenuation values below 0 since its noise .
lac_zero= size(find(LAC<0),1);
LAC(LAC<0) = 0;
% create an image of the LAC MAP
[pth,nam,ext] = spm_fileparts(CT_im.fname);
CT_im.fname = [pth filesep nam '_LAC' ext];
CT_im.dt = [16 0];
spm_write_vol(CT_im,LAC)
```

```
%% creating a sinogram of the Linear attenuation map using the
%radon transform . Create 3D sinogram space

theta = 0:179;

for slice=1:size(LAC,3)
    lac_2d = LAC(:,:,slice);

    %default 0:179
    [R,xp] = radon(lac_2d,theta);

    R_3d(:,:,slice) = R;

end

%Visualize the sinogram across all slices.
figure;
colormap gray
for slice=1:size(LAC,3)
    imshow(R_3d(:,:,slice),[],'Xdata',theta,'Ydata',xp,
                'InitialMagnification','fit')
  pause(0.3)
end

%another way to display a single slice.
%imagesc(theta,xp,R)

%% calculate the Attenuation correction factor and create
% a ACF sinogram . Do calculate the ACF we calculate the
% exponential of line integral and find the reciprocal .
```

```
ACF = exp(-R_3d);% exponential of the line integral

acf = 1./ACF;
% reciprocal of the attenuation,'Shepp-Logan' is used for the
%attenuation correction of the intensity of each voxel.

%Display ACF

figure;
colormap gray
for slice=1:size(LAC,3)
    imagesc(theta,xp,acf(:,:,slice))
    pause(0.3)
end

%Test out inverse radon

I = iradon(R,theta);
imagesc(I);

%%
% Inverse radon transform the acf--to get the acf image, just to have a
% look, but not necessary...
%figure
%I2 = iradon(acf,theta);
%imagesc(I2)

%figure; hist(acf)
%figure; hist(R)
%%
```

```
for slice=1:size(LAC,3)

    PET_2d = PET(:,:,slice);

    %default 0:179

    [P,xr] = radon(PET_2d,theta);

    pet_R_3d(:,:,slice) = P;

end

figure;
for slice=1:size(LAC,3)
    imagesc(theta,xp,pet_R_3d(:,:,slice))
    pause(0.3)
end

%%
% multiple the pet dinogram by the acf coefficients to create the
% attenuation corrected PET sinogram

att_PET_sino = pet_R_3d.*acf;

%%
% converts the sinogram inot an image
for slice=1:size(LAC,3)
    imagesc(theta,xr,att_PET_sino(:,:,slice))
    pause(0.3)
end
```

```
%Use the inverse Radon to convert back into image space

for slice = 1:size(LAC,3);

acPET_im(:,:,slice) = iradon(att_PET_sino(:,:,slice),theta,'ram-lak');
a =iradon(att_PET_sino(:,:,slice),theta);

end

%%
%acPET_im is the 3D, motion-corrected (done prior to this script),
%attentuation-corrected PET image.

[pth,nam,ext] = spm_fileparts(PET_im.fname);

%Get the scan number
 s1 = regexp(nam,'\_','split');
 sub = char(s1(3));

PET_im.fname = [pth filesep 'ac_AB_PET_fft' sub ext];
spm_write_vol(PET_im,acPET_im)
```

Appendix B

Matlab code for Standard uptake value ratio calculation

```
%This script calculates the standard uptake value ratio
%Only works for 3 images at the moment.
[inputfile1 sts]=spm_select(3, 'image', '1st PET, 2nd WM, 3rd cerebellum')
vph1=spm_vol(inputfile1(1,:));
hot1=spm_read_vols(vph1);

vph2=spm_vol(inputfile1(2,:));
hot2=spm_read_vols(vph2);

vph3=spm_vol(inputfile1(3,:));
hot3=spm_read_vols(vph3);

%Don't include NaNs in calculation of mena.
gm_cer=(~isnan(hot1)) & (hot3>0) & (hot2>0.2);



%Get mean PET value within region defined as
%cerebellar WM, GM or whole brain.
avg_pet_gm=mean(hot1(gm_cer));
```

```
%Create␣SUVR␣by␣dividing␣by␣the␣avb_pet_wm␣value.
suvr_pet=hot1/avg_pet_gm;


%**********************************
%Write␣as␣image.

[pth␣nam]=spm_fileparts(vph1.fname);
s1=regexp(nam,'\_','split');
sn=char(s1(4));
vph1.fname=[pth␣filesep␣'sum_suvr_cerebellum_GM_'␣sn␣'.nii'];
spm_write_vol(vph1,␣suvr_pet);
```

Appendix C

Copyright Agreement

ELSEVIER LICENSE TERMS AND CONDITIONS Feb 25, 2016

This is a License Agreement between Guneet Kaur ("You") and Elsevier ("Elsevier") provided by Copyright Clearance Center ("CCC"). The license consists of your order details, the terms and conditions provided by Elsevier, and the payment terms and conditions. All payments must be made in full to CCC. For payment instructions, please see information listed at the bottom of this form. Supplier Elsevier Limited The Boulevard,Langford Lane Kidlington,Oxford,OX5 1GB,UK Registered Company Number 1982084 Customer name Guneet Kaur Customer address 15a Chilcombe Street Ilam

Christchurch, 8041 License number 3816110924908 License date Feb 25, 2016 Licensed content publisher Elsevier Licensed content publication Seminars in Nuclear Medicine Licensed content title Positron Emission Tomography Radiopharmaceuticals for Imaging Brain Beta-Amyloid Licensed content author Shankar Vallabhajosula Licensed content date July 2011 Licensed content volume number 41 Licensed content issue number 4 Number of pages 17 Start Page 283 End Page 299 Type of Use reuse in a thesis/dissertation Portion figures/tables/illustrations Number of figures/tables/illustrations 1 Format electronic Are you the author of this Elsevier article? No Will you be translating? No Original figure numbers 4 Title of your thesis/dissertation Florbetben amyloid imaging for cogntive impairment in parkinson's disease Expected completion date Feb 2016 Estimated size (number of pages) 100 Elsevier VAT number GB 494 6272 12 Permissions price 0.00 USD VAT/Local Sales Tax 0.00 USD / 0.00 GBP Total 0.00 USD

References

Aarsland, D., Brønnick, K., & Fladby, T. (2011, 9). Mild cognitive impairment in parkinson's disease. *Current neurology and neuroscience report*, *11*(4), 371-378. Retrieved from http://www.ncbi.nlm.nih.gov/pubmed/21487730

Aarsland, D., & Kurz, M. W. (2010). The epidemiology of dementia associated with parkinson's disease. *Brain pathology*, *20*(3). Retrieved from http://dx.doi.org/10.1111/j.1750-3639.2009.00369.x.

Alves, G., Forsaa, E. B., Pedersen, K. F., Gjerstad, M. D., & Larsen, J. P. (2008). Epidemiology of parkinson's disease. *Journal of Neurology*, *255*(5), 18–32.

AshburnerT, J., & Friston, K. J. (2005). Unified segmentation. *NeuroImage*, *26*(4). Retrieved from http://www.fil.ion.ucl.ac.uk/~karl/Unified%20segmentation.pdf

Ay, M. R., & Sarkar, S. (2003). Computed tomography based attenuation correction in pet/ct: Principles, instrumentation, protocols, artifacts and future trends. *Iranian Journal of Nuclear Medicine*, *15*(2), 1-29. Retrieved from http://irjnm.tums.ac.ir/article_492_9a7cbebbe277c1fd0a037ee52821d378.pdf

Bach, J., Ziegler, U., Deuschl, G., Dodel, R., & Doblhammer-Reiter, G. (2011). Projected numbers of people with movement disorders in the years 2030 and 2050. *Movement Disorder*, *26*(12), 2286-2290. Retrieved from http://www.ncbi.nlm.nih.gov/pubmed/22021158

Barthel, H., Gertz, H.-J., Dresel, S., Peters, O., Bartenstein, P., & Buerger, K. (2011). Cerebral amyloid-β pet with florbetaben (18f) in patients with alzheimer's disease and healthy controls: a multicentre phase 2 diagnostic study. *The Lancet neurology*, *10*(5). Retrieved from http://dx.doi.org/10.1016/S1474-4422(11)70077-1

Basu, S., Kwee, T. C., Surti, S., Akin, E. A., & Yoo, D. (2011). Fundamental of pet and pet/ct imaging. *Annals of the New York Academy of Science*, *2011*, 1-18. Retrieved from http://dx.doi.org/10.1111/j.1749-6632.2011.06077.x

Bitar, R., Leung, G., Perng, R., & Roberts, T. P. L. (2006). Mr pulse sequences: What every radiologist wants to know but is afraid to ask1. *RADIOGRAPHICS*, *26*(2).

Retrieved from http://dx.doi.org/10.1148/rg.262055063

Braak, H., Tredici, K. D., Rüb, U., de Vos, R., Steur, E. J., & Braak, E. (2003). Staging of brain pathology related to sporadic parkinson's disease. *Neurobiology of aging*, *24*, 197-211. Retrieved from http://www.ncbi.nlm.nih.gov/pubmed/12498954

Brant-Zawadzki, Atkinson, D., Detrick, M., Bradley, W. G., & Scidmore, G. (1996). Fluid-attenuated inversion recovery (flair) for assessment of cerebral infarction. initial clinical experience in 50 patients. *Stroke*, *27*(7). Retrieved from http://dx.doi.org/10.1161/01.STR.27.7.1187

Brown, M. A., & Semelka, R. C. (2010).

In *Mri: Basic principles and applications.* Wiley-Blackwell.

Brown, M. A., & Semelka, R. C. (2011).

In *Mri: Basic principles and applications.* John Wiley and Sons.

Bushberg, J. T., Seibert, J. A., Leidholdt, E. M., & Boone, J. M. (2002).

In J. T. Bushberg (Ed.), *The essential physics of medical imaging* (3rd ed.). Lippincott Williams and Wilkins.

Campbell, M. C., Markham, J., Flores, H., Hartlein, J., Goate, A., Cairns, N. J., ... Perlmutter, J. S. (2013). Principal component analysis of pib distribution in parkinson and alzheimer diseases. *Neurology*, *81*(6), 520-527. Retrieved from http://dx.doi.org/10.1212/WNL.0b013e31829e6f94

Casey, M. E., & Nutt, R. (2007). A multicrystal two dimensional bgo detector system for positron emission tomography. *Nuclear Science, IEEE Transactions*, *33*(1). Retrieved from http://dx.doi.org/10.1109/TNS.1986.4337143

Celone, K. A., Calhoun, V. D., Dickerson, B. C., Chua, A. A. E. F., Miller, S. L., DePeau, K., ... Sperling, R. A. (2006). Alterations in memory networks in mild cognitive impairment and alzheimer's disease: An independent component analysis. *The Journal of Neuroscience*, *26*(40). Retrieved from http://dx.doi.org/10.1523/JNEUROSCI.2250-06.2006

Chao, L. L., DeCarli, C., Kriger, S., Truran, D., Zhang, Y., Laxamana, J., ... Weiner, M. W. (2013). Associations between white matter hyperintensities and β amyloid on integrity of projection, association, and limbic fiber tracts measured with diffusion

tensor mri. *PLoS ONE*, *8*(6). Retrieved from http://dx.doi.org/10.1371/journal.pone.0065175

Chaudhuri, K. R., Tolosa, E., Schapira, A. H. V., & Poewe, W. (2014). In *Non-motor symptoms of parkinsons disease.* Oxford University Press.

Cherry, S. R., Sorenson, J. A., & Phelps, M. E. (2003). In *Physics in nuclear medicine* (3rd illustration ed.). Saunders.

Comon, P. (1994). Independent component analysis, a new concept. *Signal Processing*, *36*. Retrieved from http://www.ece.ucsb.edu/wcsl/courses/ECE594/594C_F10Madhow/comon94.pdf

Compta, Y., laura Parkkinen, O'Sullivan, S. S., Vandrovcova, J., Holton, J. L., Collins, C., ... Revesz, T. (2011). Lewy- and alzheimer-type pathologies in parkinson's disease dementia: which is more important? *Brain The Journal of neurology*, *134*, 1493-1505. Retrieved from http://dx.doi.org/10.1093/brain/awr031

Dalrymple-Alford, J. C., Livingston, L., MacAskill, M. R., Graham, C., Melzer, T. R., Porter, R. J., ... Anderson, T. J. (2011a). Characterizing mild cognitive impairment in parkinson's disease. *Movement Disorder*, *26*(4), 151-153. Retrieved from http://dx.doi.org/10.1002/mds.23592

Dalrymple-Alford, J. C., Livingston, L., MacAskill, M. R., Graham, C., Melzer, T. R., Porter, R. J., ... Anderson, T. J. (2011b). Characterizing mild cognitive impairment in parkinson's disease. *Movement Disorder*, *26*(4). Retrieved from http://dx.doi.org/10.1002/mds.23592

de Lau, L., & Breteler, M. (2006). Epidemiology of parkinson's disease. *The Lancet Neurology*, *5*(6), 525-535. Retrieved from http://search.proquest.com.ezproxy.canterbury.ac.nz/docview/201444532?accountid=14499

del C. Cárdenas-Aguayo, M., del C. Silva-Lucero, M., Cortes-Ortiz, M., Jiménez-Ramos, B., Gómez-Virgilio, L., Ramírez-Rodríguez, G., ... Meraz-Ríos, M. (2014). Physiological role of amyloid beta in neural cells: The cellular trophic activity. In T. Heinbockel (Ed.), *Neurochemistry.* Retrieved from http://www.intechopen.com/books/neurochemistry/physiological-role-of-amyloid-beta-in-neural-cells-the-cellular-trophic-activity

Emre, M. (2003). Dementia associated with parkinson's disease. *THE LANCET Neurology*, *2*(6), 229-237. Retrieved from http://www.ncbi.nlm.nih.gov/pubmed/12849211

Emre, M., Aarsland, D., Brown, R., Burn, D. J., Duyckaerts, C., Mizuno, Y., ... Dubois, B. (2013). Clinical diagnostic criteria for dementia associated with parkinson's disease. *Movement Disorder*, *22*. Retrieved from http://dx.doi.org/10.1212/WNL.0b013e3182929f62.

E.Schmitz, R., Alessio, A. M., & Kinaham, P. E. (2003). *The physics of pet/ct scanners* (Vol. 2). Retrieved from http://depts.washington.edu/imreslab/education/Physics%20of%20PET.pdf

Factor, S. A., & Weiner, W. (2007).

In *Parkinson's disease: Diagnosis and clinical management*. Demos Medical Publishing.

Farncombe, T., & Iniewski, K. (2013). Pet detector. In *Medical imaging technology and applications* (chap. 11). CRC Press.

Fernandez, H. H., Crucian, G. P., Okun, M. S., Price, C. C., & Bowers, D. (2005a). Mild cognitive impairment in parkinson's disease: the challenge and the promise. *Neuropsychiatric Disease and Treatment*, *1*(1), 37-50. Retrieved from http://www.ncbi.nlm.nih.gov/pmc/articles/PMC2426819/

Fernandez, H. H., Crucian, G. P., Okun, M. S., Price, C. C., & Bowers, D. (2005b). Mild cognitive impairment in parkinson's disease: the challenge and the promise. *Neuropsychiatric disease and treatment*, *1*(1). Retrieved from http://www.ncbi.nlm.nih.gov/pmc/articles/PMC2426819/

Friedland, R. P., Kalaria, R., Berridge, M., Miraldi, F., Hedera, P., Reno, J., ... Marotta, C. A. (1997). Neuroimaging of vessel amyloid in alzheimer's disease. *Molecular neurobiology*, *826*.

Friston, K. J., Ashburner, J. T., Kiebel, S. J., E.Nichols, T., & Penny, W. D. (2011).

In K. J. Friston, J. T. Ashburner, S. J. Kiebel, T. E.Nichols, & W. D. Penny (Eds.), *Statistical parametric mapping: The analysis of functional brian images.*

Gertz, M. A., & Rajkumar, V. (2010).

In *Amyloidosis: Diagnosis and treatment*. Springer Science.

Goldman, J., & Litvan, I. (2011). Mild cognitive impairment in parkinson's disease. *Minerva Medica*, *102*(6), 441-459. Retrieved from http://www.ncbi.nlm.nih.gov/pmc/articles/PMC3370887/

Goldstein, D., Holmes, C., Sewell, L., & Kopin, I. (2009). Hypertension increases cerebral 6-18f-fluorodopa-derived radioactivity. *Journal of Nuclear Medicine*, *50*(9), 1479-1482. Retrieved from http://dx.doi.org/10.2967/jnumed.109.062869

Gomperts, S., Locascio, J., Marquie, M., Santarlasci, A. L., Rentz, D., Maye, J., ... Growdon, J. H. (2012). Brain amyloid and cognition in lewy body disease. *Movement Disorder*, *27*(8). Retrieved from http://dx.doi.org/10.1002/mds.25048

Gomperts, S., Locascio, J., & Rentz, D. (2013). Amyloid is linked to cognitive decline in patient with parkinson disease without dementia. *Neurology*, *80*(1), 85-91. Retrieved from http://dx.doi.org/10.1212/WNL.0b013e31827b1a07

Gordon, B. A., d Phillip Hsu, S. N., Roe, C. M., Morris, J. C., & Benzingera, T. L. S. (2015). The effects of white matter hyperintensities and amyloid deposition on alzheimer dementia. *NeuroImage Clincal*, *8*(1). Retrieved from http://dx.doi.org/10.1016/j.nicl.2015.04.017

Guo, S., Getsios, D., Hernandez, L., Cho, K., Lawler, E., Altincatal, A., ... Blankenburg, M. (2012). Florbetaben pet in the early diagnosis of alzheimer's disease: A discrete event simulation to explore its potential value and key data gaps. *International Journal of Alzheimer's Disease*, *2012*. Retrieved from http://dx.doi.org/10.1155/2012/548157

Hahn, E. L. (1950). Spin echoes. *Physics Review*, *80*(4). Retrieved from https://afni.nimh.nih.gov/sscc/staff/rwcox/ISMRM_2006/ISMRM%20M-F%202006/files/TuE_01.pdf

Han, J., & Luos, M. (Eds.). (2014). *Bootstrapping k-means for big data analysis.* IEEE International. doi: 10.1109/BigData.2014.7004279

Harms, S. E., Morgan, T. J., Yamanashi, W. S., Harle, T. S., & Dodd, G. D. (1984). Principles of nuclear magnetic resonance imaging. *RSNA Radiographics*, *4*(1). Retrieved from http://dx.doi.org/10.1148/radiographics.4.1.26

Hashemi, R. H., Bradley, W. G., & Lisanti, C. J. (2012).

In *Mri: The basics.* Lippincott Williams and Wilkins.

Hendrick, E. R. (2007).

In *Breast mri fundamentals and technical aspects.* Springer.

Hyvärinen, A., & Oja, E. (2000). Independent component analysis: Algorithms and applications. *Neural Networks*, *13*(4-5). Retrieved from https://www.cs.helsinki.fi/u/ahyvarin/papers/NN00new.pdf

Iniewski, K. (2009).

In *Medical imaging: Principles, detectors, and electronics.* John Wiley and Sons.

Jellinger, K. A. (2010a). The neuropathologic substrate of parkinson disease dementia. *Acta Neuropathologica*, *119*(1), 151-153. Retrieved from http://dx.doi.org/10.1007/s00401-009-0613-1

Jellinger, K. A. (2010b). Neuropathology in parkinson's disease with mild cognitive impairment. *Alzheimer's research and therapy*, *120*(6). Retrieved from http://dx.doi.org/10.1007/s00401-010-0755-1

Katz, D. I., Zafonte, R. D., & Zasle, N. D. (2006).

In *Brain injury medicine: Principles and practice.* Demos Medical Publishing.

Kinahan, P. E., Hasegawa, B. H., & Beyer, T. (2003). X-ray-based attenuation correction for positron emission tomography/computed tomography scanners. *Seminars in nuclear medicine*, *33*(3). Retrieved from http://dx.doi.org/10.1053/snuc.2003.127307

Litvan, I., Goldman, J. G., I.Troster, A., Schmand, B. A., Weintraub, D., Petersen, R. C., ... Emre, M. (2012). Diagnostic criteria for mild cognitive impairment in parkinson's disease: Movement disorder society task force guidelines. *Movement Disorder*, *27*(3), 349-356. Retrieved from http://www.ncbi.nlm.nih.gov/pubmed/22275317

Litvan, I., Goldman, J. G., Tröster, A. I., Schmand, B. A., Weintraub, D., Petersen, R. C., ... Emre, M. (2012). Diagnostic criteria for mild cognitive impairment in parkinson's disease: Movement disorder society task force guidelines. *Movement Disorder*, *27*(3). Retrieved from http://dx.doi.org/10.1002/mds.24893

Madhavi, T. (2014).

In T. Madhavi (Ed.), *Inflammation in parkinson's disease : Scientific and clinical aspects.*

MA.Hely, Reid, W., Adena, M., Halliday, G., & Morris, J. (2008). The sydney multicenter study of parkinson's disease: the inevitability of dementia at 20 years. *Movement Disorder*, *23*, 837-844. Retrieved from http://dx.doi.org/10.1002/mds.21956

MathWorks. (2015). *Radon transform.* Retrieved from http://au.mathworks.com/help/images/radon-transform.html

McRobbie, D. W., Moore, E. A., Groves, M. J., & Prince, M. R. (2007).

In *Mri: from picture to proton.* Cambridge.

Melzer, T. R., Watts, R., Macaskill, M., Pitcher, T. L., Livingston, L., & Keenan, R. (2012). Grey matter atrophy in cognitively impaired parkinson's disease. *Journal of Neurology, Neurosurgery and Psychiatry*, *83*(2). Retrieved from http://dx.doi.org/10.1136/jnnp-2011-300828

Melzer, T. R., Watts, R., Macaskill, M., Pitcher, T. L., Livingston, L., Keenan, R., ... Anderson, T. J. (2013). White matter microstructure deteriorates across cognitive stages in parkinson disease. *Neurology*, *80*(20). Retrieved from http://dx.doi.org/10.1212/WNL.0b013e3182929f62.

Mendez, M. F., & Cummings, J. L. (2003).

In *Dementia: A clinical approach.* Butterworth-Heinemann.

Mikla, V. I., & Mikla, V. V. (2013).

In *Medical imaging technology.* Elsevier.

Palavra, N. C., Naismith, S. L., & Lewis, S. J. G. (2013). Mild cognitive impairment in parkinson's disease: A review of current concepts. *Neurology Research International*, *2013*, 8. Retrieved from http://dx.doi.org/10.1155/2013/576091

Pearson, H. A., & Peers, C. (2006). Physiological roles for amyloid β peptides. *The Journal of Physiology*, *575*(1), 5-10. Retrieved from http://doi.org/10.1113/jphysiol.2006.111203

Pedersen, K. F., Larsen, J. P., Tysnes, O.-B., & Alves, G. (2013). Prognosis of mild cognitive impairment in early parkinson disease: the norwegian parkwest

study. *JAMA neurology*, *70*(5), 580- 586. Retrieved from http://dx.doi.org/10.1001/jamaneurol.2013.2110

Petroou, M., Bohnen, N. I., Muller, M., Albin, R., & Frey, K. (2012). Aβ-amyloid deposition in patients with parkinson disease at risk for development of dementia. *Neurology*, *79*(11), 1161-1167. Retrieved from http://dx.doi.org/10.1212/WNL.0b013e3182698d4a

Phelps, M. E. (2004).

In *Molecular imaging and its biological applications.* Springer Science and Business Media.

Phelps, M. E. (2006).

In *Pet: Physics, instrumentation, and scanners.* Springer Science and Business Media.

Potecorvo, M. J., & Mintun, M. A. (2011). Pet amyloid imaging as a tool for early diagnosis and identifying patients at risk for progression to alzheimer's disease. *Alzheimer's research and therapy*, *3*(2). Retrieved from http://dx.doi.org/10.1186/alzrt70

Pringsheim, T., Jette, N., Frolkis, A., & Steeves, T. (2014). The prevalence of parkinson's disease: A systematic review and meta-analysis. *Movement Disorder*, *29*(13), 1583–1590. doi: http://dx.doi.org/10.1002/mds.25945

Quinn, J. F. (2014).

In *Dementia.* John Wiley and Son. Ltd.

Rencher, A. C., & Christensen, W. F. (2012).

In *Methods of multivariate analysis.* John Wiley and Sons.

Rich, K. M. W., & Christian, P. E. (2013).

In *Nuclear medicine and pet/ct: Technology and techniques.* Elsevier Health Sciences.

Richards, D., & Sabbagh, M. N. (2014). Florbetaben for pet imaging of beta-amyloid plaques in the brain. *Neurology and Therapy*, *3*(2). Retrieved from http://dx.doi.org/10.1007/s40120-014-0022-9

Ross, S., & Stearnsr, C. (2016). Sharpir white paper. *GE health*. Retrieved from http://www.gehealthcare.com

Saha, G. B. (2015).

In *Basics of pet imaging: Physics, chemistry, and regulations.* Springer.

Samii, D. A., Nutt, P. J. G., & Ransom, P. B. R. (2004). Parkinson's disease. *The Lancet*, *363*(9423), 1783 - 1793. Retrieved from http://dx.doi.org/10.1016/S0140-6736(04)16305-8

Selkoe, D. J. (2004). Cell biology of protein misfolding: The examples of alzheimer's and parkinson's diseases. *Nature Cell Biology*, *6*, 1054-1061. Retrieved from http://www.nature.com/ncb/journal/v6/n11/full/ncb1104-1054.html

Silbert, L. C., & Kaye, J. (2010). Neuroimaging and cognition in parkinson's disease dementia. *Brain Pathology*, *20*(3). Retrieved from http://dx.doi.org/10.1111/j.1750-3639.2009.00368.x.

Striet, R. L. (2010). Tomographic imaging. In *Poisson point processes: Imaging, tracking, and sensing* (p. 110-134). Springer Science and Business Media.

Stühler, E., & Merhof, D. (n.d.). Principal component analysis applied to spect and pet data of dementia patients – a review. In P. Sanguansat (Ed.), *Numerical analysis and scientific computing.*

Thomas, B., & Beal, M. F. (2007). Parkinson's disease. *Human Mollecular Genetics*, *16*(2), 183-194. Retrieved from http://hmg.oxfordjournals.org/content/16/R2/R183.full.pdf

Vallabhajosula, S. (2011). Positron emission tomography radiopharmaceuticals for imaging brain beta-amyloid. *Alzheimer's research and therapy*, *3*(2). Retrieved from http://dx.doi.org/10.1053/j.semnuclmed.2011.02.005

Villemagne, V. L., Mulligan, R. S., Pejoska, S., Ong, K., Jones, G., O'Keefe, G., ... Danguy, H. T. (2012). Comparison of 11c-pib and 18f-florbetaben for aβ imaging in ageing and alzheimer's disease. *European Journal of Nuclear Medicine and Molecular Imaging*, *36*(6). Retrieved from http://dx.doi.org/10.1007/s00259-012-2088-x

Weishaupt, D., Köchli, V. D., & Marincek, B. (2006). In *How does mri work? an introduction to the physics and function of magnetic resonance imaging.* Springer.

Wood, K.-L., Myall, D. J., Livingston, L., Melzer, T. R., Pitcher, T. L., MacAskill, M. R., ...

Dalrymple-Alford, J. C. (2016). Different pd-mci criteria and risk of dementia in parkinson's disease: 4-year longitudinal study. *npj Parkinson's disease*, *2*. Retrieved from http://dx.doi.org/10.1038/npjparkd.2015.27

Yarnall, A., Rochester, L., & Burn, D. (2013). Mild cognitive impairment in parkinson's disease. *Age and Aging*, *42*(5), 567-76. Retrieved from http://www.ncbi.nlm.nih.gov/pubmed/23868092

Zeng, D. G. L. (2010).

In *Medical image reconstruction.* Springer Berlin Heidelberg.

Ziegler, S. I. (2005). Positron emission tomography: principle, technology and recent developments. *Nuclear Physics*, *752*(1). Retrieved from http://dx.doi.org/10.1212/10.1016/j.nuclphysa.2005.02.067